Tectonophysics 898 (2025) 230641

Contents lists available at ScienceDirect

Tectonophysics

journal homepage: www.elsevier.com/locate/tecto

The complex 4D multi-segmented rupture of the 2014 M_w 6.2 Northern Nagano Earthquake revealed by high-precision aftershock locations

Titouan Muzellec [a,*], Grazia De Landro [a], Giovanni Camanni [b], Guido Maria Adinolfi [c], Aldo Zollo [a]

[a] Università degli Studi di Napoli "Federico II", Dipartimento di Fisica E. Pancini, RISSC-Lab, Naples, Italy
[b] Dipartimento di Scienze Chimiche e Geologiche, Università di Modena e Reggio Emilia, Modena, Italy
[c] Università degli Studi di Torino, Dipartimento di Scienze della Terra, Turin, Italy

ARTICLE INFO

Keywords:
Nagano earthquake sequence
Earthquake rupture
4D seismicity distribution
Multisegmented fault surface

ABSTRACT

Enhanced earthquake sequence seismic catalogs have the potential to reveal fault surface complexities at depth (e.g., segmentation, bends). Past analyses were generally restricted to 2D analysis considering faults discontinuous along their strike and do not include segment temporal evolution. Our work provides a comprehensive methodology, for reconstructing the 3D fine-scale (few kilometers length) geometry of a segmented fault surface and to characterize the triggering of the segments during an earthquake mainshock-aftershock sequence *We* analyzed the 2014 Northern Nagano (Japan) (M_w 6.2) earthquake sequence using high-resolution seismic catalogs. We automatically detected and located about 2500 events between October and December 2014 with a magnitude range between –0.6 and 6.2. We refined the automatic picks, based on cross-correlation and hierarchical clustering, and we relocated the hypocenters with the double-difference technique in 3D velocity models optimized for the area. Moreover, we calculated the composite focal mechanisms of the main clusters, crucial to constrain the kinematics and the 3D geometry of the fault segments, and rupture directivity that we interpreted jointly with the seismicity and the fault slip. We find that a segmented fault surface comprising, at least, 9 distinct segments, ruptured during 3 successive activation phases. The different segments exhibit a different rupture mechanism based on their spatial and temporal occurrence, influencing seismicity evolution and rupture length. Our method, based on deep analysis of relocated aftershocks sequence, can be used in other study cases for the fault surface reconstruction to better understand the complexity of the earthquake rupture.

1. Introduction

Faults in 3D are rarely individual planar surfaces whereas they are most often comprised of multiple fault segments, with each segment having different mechanical properties and geometries that can be vary along the strike and the dip of a fault (e.g., Walsh et al., 2003; Marchal et al., 2003; Kristensen et al., 2008; Tvedt et al., 2013; Seebeck et al., 2015; Lăpădat et al., 2017; Collanega et al., 2019; Camanni et al., 2019; Camanni et al., 2023a, 2023b; Deng et al., 2020; Delogkos et al., 2020; Roche et al., 2021). In active tectonics settings, fault segmentation is generally acknowledged along the strike of faults analyzed in 2D map views (King and Nábělek, 1985; Barka and Kadinsky-Cade, 1988; Wesnousky, 1988; Stirling et al., 1996; Manighetti et al., 2007, 2009; Perrin et al., 2016; Hamling et al., 2017). Nevertheless, when projected at depth, active faults are usually simplified or modeled as sub-vertical planar features (Cockerham and Eaton, 1987; Schaff et al., 2002; Graymer et al., 2007; Waldhauser and Schaff, 2008; Savran and Olsen, 2020; Ramos et al., 2022), with the exception of the addition of the primary overlap zones between segments or fault bends that are, however, most often extrapolated at depth maintaining a similar geometry to the one they have at the surface (Hu et al., 2016; Tondi et al., 2020; Huang et al., 2023; Tung et al., 2024). The reconstruction of a correct model for the segmentation of fault surfaces and earthquake rupture zones at seismogenic depths is crucial for a deeper understanding of earthquake rupture physics (Wesnousky, 2008; Savran and Olsen, 2020; Ramos et al., 2022; Palo et al., 2023) with significant implications for earthquake hazard assessment (Buttinelli et al., 2021). Indeed, fault segments interaction during the rupture and their mutual static stress triggering is a prominent mechanical process during the sequence, whose impact could affect the hazard scenario (Iacoletti et al., 2021;

* Corresponding author.
E-mail address: titouan.muzellec@unina.it (T. Muzellec).

https://doi.org/10.1016/j.tecto.2025.230641
Received 31 May 2024; Received in revised form 24 January 2025; Accepted 25 January 2025
Available online 27 January 2025

Howell et al., 2024).

In recent years, there has been an increased possibility of building-up enhanced seismic catalogs, rich in events that are precisely located (especially small magnitude ones; Meng and Ben-Zion, 2018; Spallarossa et al., 2021; Stabile et al., 2021; Scotto di Uccio et al., 2023, 2024). These enhanced catalogs have significant potential in revealing previously neglected structural complexities of fault geometries at seismogenic depth, to attempt overcoming the above-mentioned limitations (Panayotopoulos et al., 2016; Piegari et al., 2024; Scotto di Uccio et al., 2024). Complemented with geological data, these enhanced catalogs potentially can allow (i) to derive a realistic image of the 3D segmentation of active fault surfaces by recognising the geometry of its primary fault segments. In addition, they also allow (ii) to determine the spatio-temporal activation of these fault segments during an earthquake (Cesca et al., 2017; Ross et al., 2019), as well as (iii) their precise orientation and kinematics through the calculation of earthquake focal mechanisms (Bailey et al., 2010; Camanni et al., 2014). In this work, we provide a comprehensive and integrated approach to reconstruct the 3D segmented (few kilometers length) geometry of a fault surface and the evolution of segments activation (i.e., fourth dimension) starting from an enhanced catalog of mainshock-aftershock sequence over a time interval extending beyond the early aftershocks (i.e., several months). We selected the November 2014 Northern Nagano earthquake (M_w 6.2), Japan, as it involved a prolonged and complex aftershock sequence associated with more than 2000 events on a complex segmented fault surface (Panayotopoulos et al., 2016; Imanishi and Uchide, 2017). Initially, we built an enhanced seismic catalog by applying a procedure for the event detection and location to the continuous data from 22 November to 31 December 2014. Successively, we refined the automatic absolute picks with a new technique based on waveform similarity and hierarchical clustering. The high-precision earthquake locations were obtained by double difference (DD) technique and 3D velocity models optimized for the area. The seismicity pattern, combined with newly calculated composite focal mechanisms of significant clusters, were in turn used to derive the 3D geometry of the different fault segments activated during the mainshock rupture and in the following weeks. By adding considerations on the time, these data provided a new model of the 4D occurrence and clustering of events that characterize the rupture evolution of the complex fault surface during 3 main phases of the 2014 Nagano earthquake sequence.

2. Geological setting of the Mw 6.2 Northern Nagano Earthquake sequence

The tectonic setting of the study area is dominated by the Itoigawa-Shizuoka tectonic line (ISTL), which crosses Honshu Island and extends for ~150 km from Itoigawa City on the Sea of Japan to Shizuoka City on the Pacific Ocean (see Fig. 1). The ISTL, which roughly strikes NNE–SSW

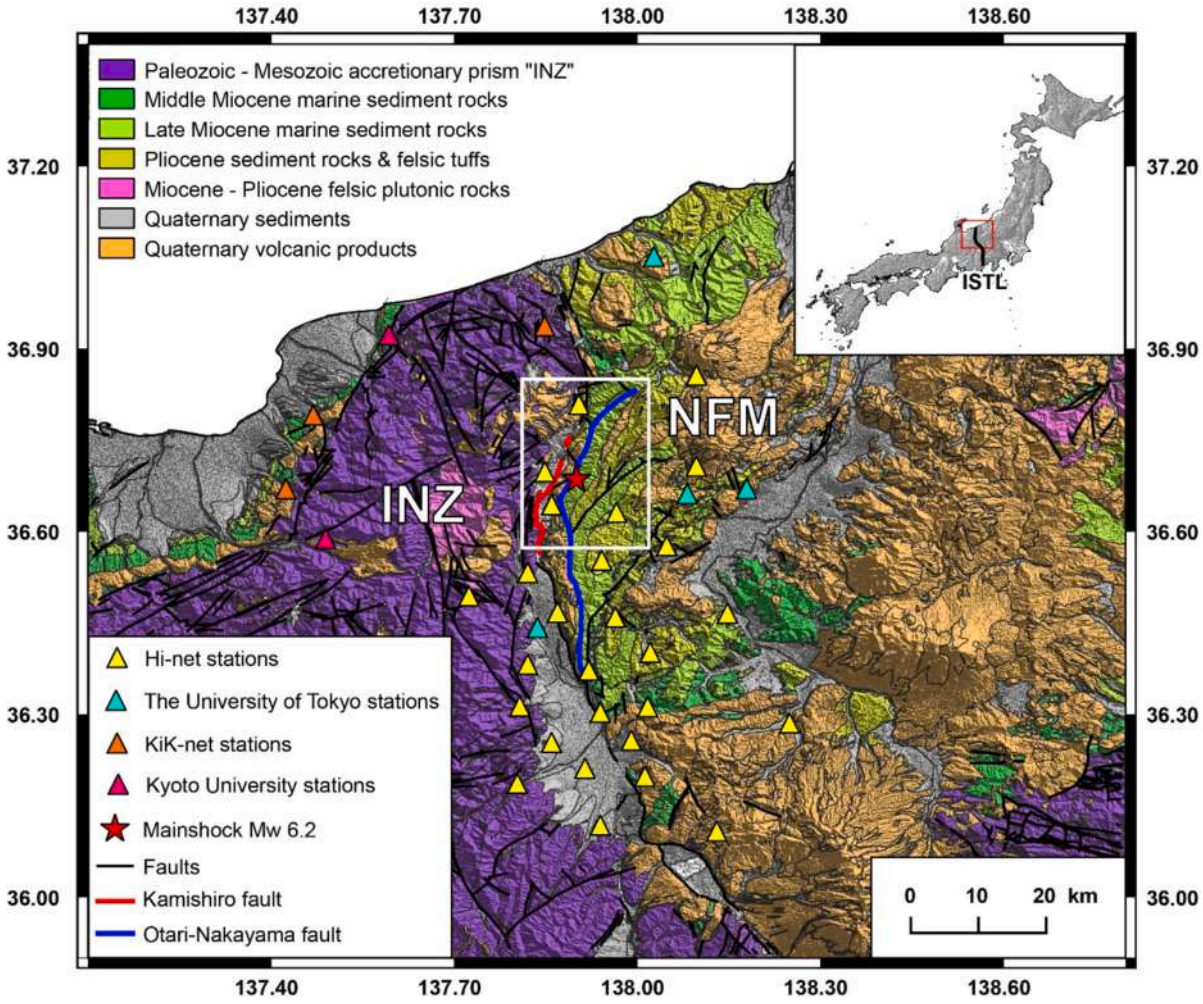

Fig. 1. Geological map of the area surrounding the 2014 Nagano earthquake sequence, modified from Panayotopoulos et al. (2016). Red star indicates the M_w 6.2 mainshock location. Triangles indicate the location of the seismic stations used in this study. White rectangle indicates the study area. Northern Fossa Magna (NFM), Inner Zone (INZ), Itoigawa-Shizuoka tectonic line (ISTL). (For interpretation of the references to colour in this figure legend, the reader is referred to the web version of this article.)

to NNW–SSE, is one of the most active faults in Japan; it corresponds to one arm of the triple junction between the Eurasian, North American, and Philippine Sea plates. In the North, within the study area, the ISTL is made up of at least two major, nearly N-S striking, sub-parallel branches: the Kamishiro fault (KF, Fig. 1) in the West, and the Otari–Nakayama fault (OTNF, Fig. 1) in the East. Both faults developed as the bounding, east-dipping extensional faults of the Northern Fossa Magna (NFM) rift basin (Sato, 1994), which formed during the final extensional stages of the opening of the Japan Sea (25–15 *Ma*) (Otofuji et al., 1985; Yamaji, 1990), and juxtapose sedimentary rocks of the basin infill in the East against older basement rocks of the "inner zone" (INZ) in the West. The NFM basin comprises 5–6 km thick Miocene marine sediments (Kato, 1992; Takano, 2002; Panayotopoulos et al., 2013); the INZ is largely made up of pre-Neogene basements rocks comprising Paleozoic-Mesozoic accretionary complex and granitic rocks (Fig. 1) (Kano et al., 1990; Taira, 2001).

Since the Pliocene (ca. 3 Ma) an inversion of the stress field in central Japan resulted in the ongoing inversion of the NFM rift basin through the reactivation of its bounding fault system with overall reverse faulting (Williams et al., 1989; Sato, 1994; Sato, 1996). The KF has been shown to be currently an active thrust fault (e.g., Sato et al., 2004; Takeda et al., 2004). On the other hand, the OTNF, shows no geomorphological evidence of late Quaternary activity (Matsuta et al., 2004).

The M_w 6.2 mainshock of the seismic sequence studied here occurred at the Northern Nagano prefecture on the 22 November 2014 at 10:08 pm JST (01:08 pm UTC). The epicenter of the mainshock is located nearby the KF and OTNF faults (red star in Fig. 1), and the estimated focal mechanism from the centroid moment tensor (CMT) solution, given by the Japan Meteorological Agency (JMA) and by the National Research Institute for Earth Science and Disaster Resilience (NIED), shows a reverse fault with a left-lateral component (Japan Meteorological Agency, 2014; National Research Institute for Earth Science and Disaster Prevention, 2014). Foreshock activity was detected near the mainshock location during the 4 days before its occurrence. Imanishi and Uchide (2017) indicate that the 4D evolution of the foreshock activity is characterized by seismicity migration from the shallow crust to the mainshock location. Imanishi and Uchide (2017) interpreted the mainshock to have been triggered by stress loading caused by the foreshock activity driven by aseismic slow slip.

Most of the surface ruptures related to the mainshock followed the mapped surface trace of the KF (Okada et al., 2015). Several studies used interferometric synthetic-aperture radar (InSAR) (Panayotopoulos et al., 2016; Ando et al., 2017; Kobayashi et al., 2018) to identify the surface displacement observed after the mainshock and interpreted the slip distribution to be associated with a non-planar east-dipping fault formed by KF and OTNF faults. Similarly, by using the relocated hypocenter of a part of the aftershock activity, Panayotopoulos et al. (2016) determined the source fault model to be composite, with a shallow part corresponding to the KF with a dip of 30°-45°, and a deeper portion corresponding to the deep part of the OTNF with a dip of 50°-60°, resulting in an overall bending, steepening downward fault planar surface. Ando et al. (2017) confirmed this downward steepening fault structure and added branch faults with different bends for the different clusters around the main fault to approximately fit the surface deformation data. The aftershocks relocated by Panayotopoulos et al. (2016) show a clear difference in seismicity distribution between the northern and the southern part of the earthquake sequence area. The gap of aftershocks on the surface rupture is consistent with several studies showing aftershocks concentration at the margin of an asperity (Okada et al., 2015), where the coseismic slip is low (Panayotopoulos et al., 2016). Indeed, Ando et al. (2017) show a high coseismic slip patch in the south of the earthquake sequence at shallow depth. This correlation of high slip patch on the fault and low concentration of aftershocks, which has been observed for other major earthquakes in Japan (Hirata et al., 1996; Asano et al., 2011), is related to the total stress release on this patch of the fault.

3. Data and methods

3.1. Refinement picking

In this study we used continuous seismic data recorded from 22 November to 31 December 2014 by 27 short period three component velocity seismometers of the permanent network Hi-net (National Research Institute for Earth Science and Disaster Resilience, 2019) operated by the NIED and JMA, 4 seismometers operated by the University of Tokyo, 3 strong-motion seismograms of the permanent network KiK-net and 2 seismometers operated by Kyoto University (triangles in Fig. 1). First, we applied an optimization strategy to join existing methods for the automatic detection (Adinolfi et al., 2020), picking, and location of events; then we used LASSIE (Heimann et al., 2017) PHASE (Ross and Ben-Zion, 2014) and MParloc (Zollo et al., 2021), respectively, following the same approach as Adinolfi et al. (2020, 2022, 2023). This allowed us to construct a homogeneous initial catalog of 2477 events for the entire period of three months with a magnitude range between –0.6 and 6.2 (see Fig. S1 in SM).

It is well known that automatic picking tools can introduce systematic shifts to the output pick distribution (Lois et al., 2013; Baillard et al., 2014). This affects, not only the quality of the initial catalog location, but also the accuracy of differential travel-time measurements, that depend on the event origin time. To obtain high quality DD locations, we applied a refined picking procedure based on waveform similarity and hierarchical clustering, for the first set of automatic absolute picks. Using cross-correlation (CC) we measured the similarity between waveforms of the filtered seismic records to build families of similar events with hierarchical clustering. Within each family, we constructed a reference trace (RT), by the weighted stack of all the waveforms, on which automatically measured a refined pick used as reference to correct the picks of other events in the family (for further details see section A1 in SM). This procedure is constructed to mitigate both the inconsistency among picks on similar waveforms and the systematic shift introduced by automatic picking tools (Fig. 2a). By calculating the increase of signal to noise ratio (SNR) for refined picks, versus initial picks, (Fig. S2 in SM) we show an improvement in our pick quality.

3.2. Earthquake locations

To improve the hypocenter location, we followed a three steps process:

1) First, we estimated the absolute hypocenter locations with NonLinLoc software (Lomax et al., 2009) in the 1D velocity model used for the JMA Unified Earthquake Catalog (Japan Meteorological Agency, 2014), by inverting initial automatic picks and refined picks. Then we relocated the seismicity in DD by using HypoDD (Waldhauser and Ellsworth, 2000) which invert iteratively the CC and catalog differential times. The CC differential travel times were calculated between events within families built during the refinement picking procedure.
2) To further improve our location quality, we constructed 3D P- and S-waves velocity models by inverting arrival times through a linearized tomographic approach. We used the code TOMOTV (Latorre et al., 2004), well established since applied in different environments and at different scales (De Landro et al., 2020, 2022; Amoroso et al., 2022). In our workflow, we inverted the refined picks by starting from the 1D velocity model from JMA (Japan Meteorological Agency, 2014) (see section A2 in SM). In map view, there is a strong east-west variation of velocity in the first 5 km depth (Fig. S3.1–2). The geological structure characterized by a low velocity on the eastern side of the fault system should end between 4 and 7 km depth. By comparing the position of the velocity anomalies and the geological features at the surface, the low velocity anomaly on the east side of the fault system is related to the NFM basin, while the

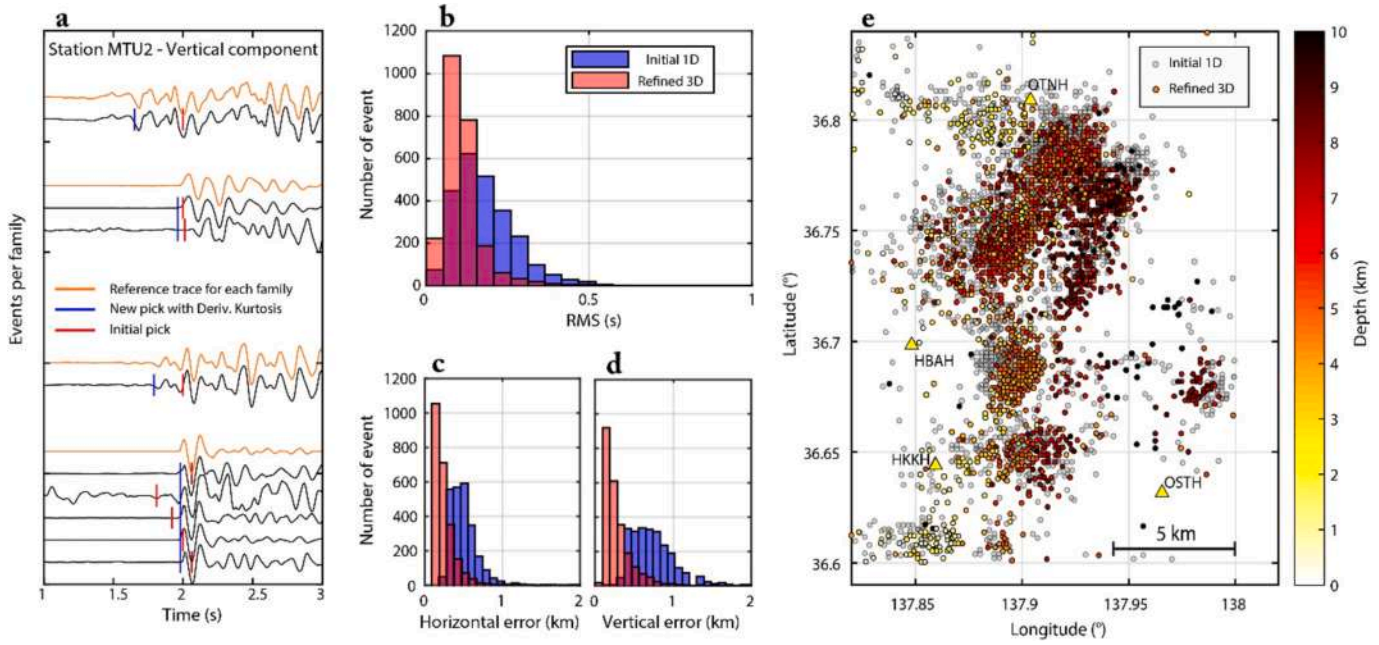

Fig. 2. (a) Seismic traces recorded on the vertical component at one station classified by family. The orange trace is the RT of each family. Vertical blue line indicates the position of the refined P arrival time. Vertical red line indicates the position of the initial P arrival time. (b) Histogram of the root mean square (RMS) from the absolute locations. (c) Same as be for the horizontal error. (d) Same as (b) for the vertical error. (e) Relocation absolute of the seismicity of the 2014 Nagano earthquake sequence by using the 1D/3D velocity models and the initial/refined arrival time picks. (For interpretation of the references to colour in this figure legend, the reader is referred to the web version of this article.)

high velocity anomaly of the west side of the fault corresponds to the INZ (basement structure).

3) In the next step, we located the hypocenters in 3D velocity models (Fig. S3.1–2 in SM) with NonLinLoc (Lomax et al., 2009), we computed the CC differential times by considering refined locations and, then we relocated the seismicity with HypoDD by inverting CC and catalog differential times (see section A2 in SM).

The consistency of the refined phase picks allowed us to increase the accuracy of absolute location by reducing the root-mean-square (RMS) from 0.19 s to 0.11 s (Fig. 2b) and the mean location error from 0.6 km to 0.2 km (Fig. 2c-d). This result is a further confirmation of the improvement of pick quality due to the application of the refined procedure. It is interesting to note that with 3D absolute locations we observed a clustering of events and a shift of the seismicity toward the east compared with the previously observed hypocenters derived from the use of DD location (Fig. 2d; Panayotopoulos et al., 2016). To minimize the effect of the global harmonization of the 3D model at large parameterization, we focused the analysis on the hypocenter locations determined by relative travel times based on their location within the 3D velocity model. With the last location step, we reduced the location errors for DD to an average of about 100 m (see section A2 and Fig. S4 in SM).

3.3. Rupture directivity

We used the 23 strong motion records of the M_w 6.2 Northern Nagano earthquake acquired by near-source strong-motion seismographs from the Kiban Kyoshin network (KiK-net) operated by the NIED (National Research Institute for Earth Science and Disaster Resilience, 2019) to infer the mainshock rupture geometry and propagation mode (uni- or bi-lateral) (see section A3 and Fig. S5 in SM). The method proposed by Convertito et al. (2012) has been applied to invert the recorded Peak Ground Velocity (PGV) data to determine the fault length (in terms of its surface projection), together with the dominant rupture mode, rupture direction and rupture velocity.

For this analysis we assumed a moment magnitude M_w 6.2 for the mainshock and used the PGV data measured from the 0.1–3 Hz band-pass filtered accelerograms recorded by the 23 near-source stations of the strong motion network. PGV data are preliminary corrected for the distance attenuation effect, by multiplying each event by the hypocentral distance, then the optimal rupture parameters (rupture length L, predominant rupture length L', Mach number α and the rupture direction) are determined through a Bayesian probabilistic inversion method based on a grid search model parameter exploration (Convertito et al., 2012). The final PGV residual distribution confirms the consistency of the retrieved model with observations indicating a well peaked residual distribution around zero with a net improvement relative to the directivity of un-modeled data (see Fig. S5 in SM).

3.4. Composite focal mechanisms

To determine the detailed fault geometry and confirm the fault delineation highlighted by the seismicity, we computed the composite focal mechanism with the program FPFIT (Reasenberg, 1985) for several clusters by reducing the uncertainty of the polarity measurements for single events. Using the polarity measurements of each event among the same cluster, FPFIT calculates the best fault-plane solution with a weighted sum of the first P-wave polarity discrepancies (Aki and Richards, 2002). For this analysis, we evaluate the composite focal mechanism by selecting co-located events belonging to 9 significant clusters with a total of 1053 events. We selected the clusters based on the event's 4D proximity, by focusing on the small-scale clusters of the seismicity pattern not detected in previous works (Panayotopoulos et al., 2016). We manually measured the polarities at least for the 8 closest seismic stations from the earthquake sequence location. The results can be found in table S1 of SM. The obtained focal mechanisms are well constrained, and the average error in strike, dip, and rake is about 7°, 11°, and 12°, respectively (see Fig. S6–14 in SM).

4. 4D seismicity distribution and rupture evolution

Hypocenters of the relocated mainshock and aftershocks are shown in Figs. 3, 4, and 5. In Fig. 3 we show the map view, the cross sections, and distance along fault strike of aftershocks versus time over the entire sample period. The mainshock of the Nagano sequence occurred on 22 November 2014 at 01:08:17.56 pm (UTC) at 3.3 km of depth on the northern tip of the southern segment involved in the rupture (red star in Fig. 3,4a-b). The relocation procedure allowed us to reach an unprecedented precision in the location of the mainshock, with location errors of the order of a few hundred meters (see section A2 in SM). Looking at the aftershock epicentral distribution (Fig. 3), we note that the distribution follows structures striking N20°, with a higher number of aftershocks in the northern part of the earthquake sequence compared to the southern part. In the cross sections, most of the aftershocks are distributed in several clusters that we can clearly identified (see sections on Fig. 3). In the southern area of aftershocks, the seismicity follows a single fault plane with a main cluster around the mainshock location. In the northern area, the clusters identified are globally deeper than the clusters identified in the southern area.

Also, we note that some clusters were activated by a major aftershock (with a $M_{JMA} \geq 4$, green stars on Fig. 3). The temporal distribution of

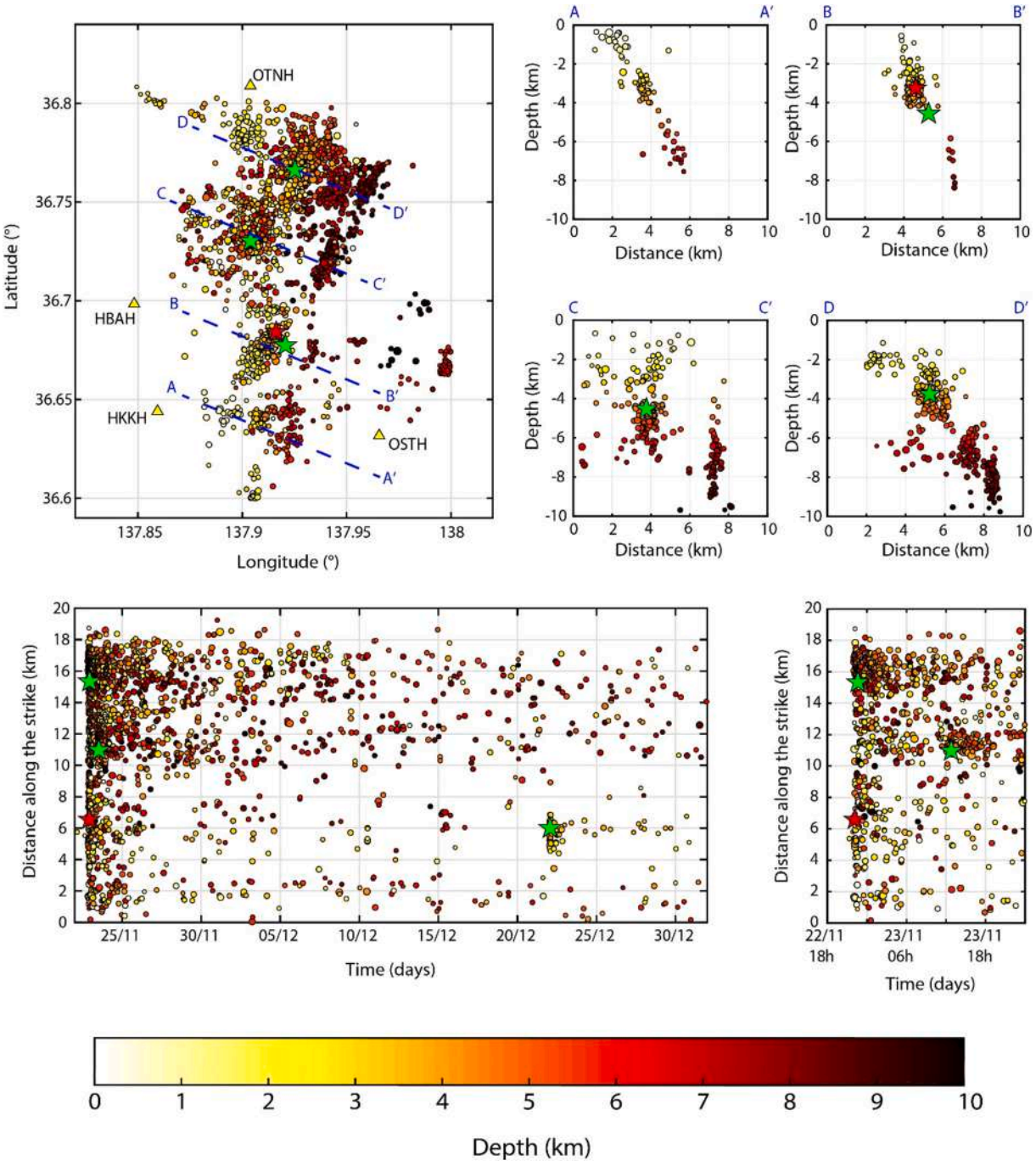

Fig. 3. Map view, sections, and distribution of the seismicity along strike versus time during the entire period of the earthquake sequence. Red star denotes the M_w 6.2 mainshock and the green stars correspond to the major aftershock with a $M_{JMA} \geq 4$. Circles denote aftershocks and sizes scale with magnitudes. Yellow triangles are the seismic stations. The colour bar indicates the depth of aftershocks. The blue dash lines indicate the positions of sections A-A', B-B', C-C' and D-D′. (For interpretation of the references to colour in this figure legend, the reader is referred to the web version of this article.)

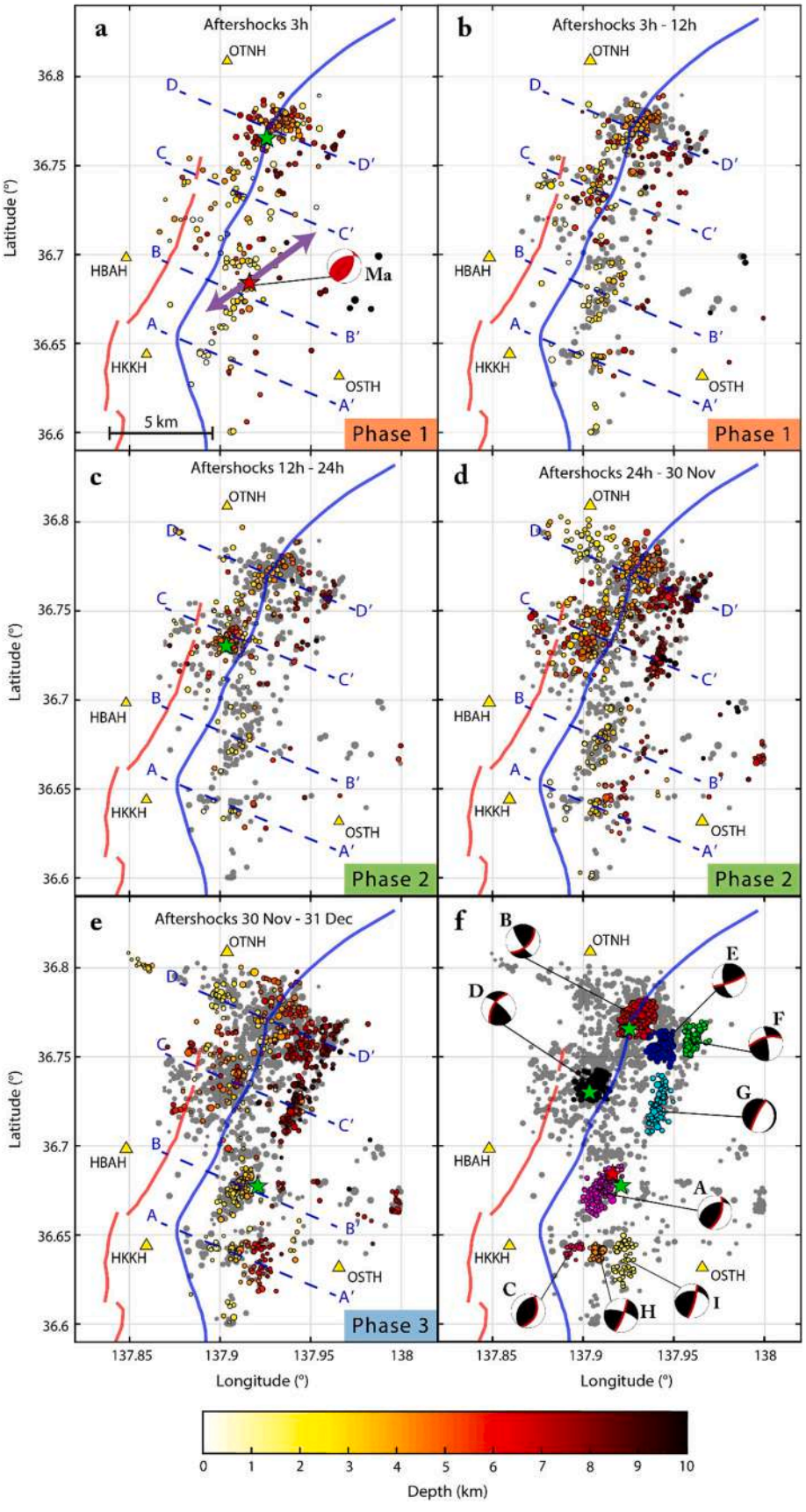

(caption on next page)

Fig. 4. Spatial and temporal distribution of the aftershock sequence at different time periods after relocation (a-b) aftershocks in phase 1 of the aftershock sequence, (c-d) phase 2 and (e) phase 3 and the composite focal mechanism for each individual cluster. Red star denotes the mainshock and the green stars correspond to the major aftershocks with a $M_{JMA} \geq 4$. Filled circles denote aftershocks with circle size scaling to magnitude. Gray circles correspond to the aftershocks which occurred before the time interval shown in each map. Yellow triangles are seismic stations. The colour of aftershock filled circles denotes depth of the aftershocks (see colour bar for depths). The blue dash lines indicate the position of the sections. The focal mechanism represented in red is the CMT solution for the mainshock estimated by NIED using F-net. The red and blues lines on the map correspond to the fault traces at the surface for the Kamishiro fault and the Otari-Nakayama fault, respectively. The purple arrows indicate the rupture directivity and the rupture mode of the mainshock. The index letters of each composite focal mechanism are referred to Table S1 in SM. The red line on each focal mechanism corresponds to the interpreted fault plane. The time periods for each phase are (see Table 1): a) from MOT to 3 h after; b) from 3 h to 12 h after; c) from 12 h to 24 h after MOT; d) from 24 h to one week after MOT; e) from one week after the MOT to one month after MOT. (For interpretation of the references to colour in this figure legend, the reader is referred to the web version of this article.)

seismicity along strike (Fig. 3) shows the temporal clustering only for the shallower clusters/segments activated by a major aftershock. The aftershocks distribution among several clusters/segments, activated at different times and were probably affected by several triggering mechanisms, show the complexity of the main rupture.

To constrain the geometry of the faults involved in the Nagano sequence, previous analyses have been based on the calculation of focal mechanisms for major aftershocks in different sectors of the system (Japan Meteorological Agency, 2014; National Research Institute for Earth Science and Disaster Resilience, 2019; Panayotopoulos et al., 2016).

To characterize the temporal pattern of the seismicity of fault segments, we selected 4 different time intervals based on the variation of the seismicity distribution (see table 1) in Figs. 4 and 5.

By analyzing the seismicity within the different time intervals (Figs. 4 and 5), we define 3 main phases with the first phase of seismicity occurring coseismically and within the 12 h of the main rupture, the second phase, within a week of the mainshock, characterized by activation of deep segments in the northern area, and the third phase within a month of the mainshock, characterized by activation of the deep part of the fault in the southern area.

4.1. Phase 1 / Mainshock rupture

The early aftershocks which highlight the geometry of the mainshock rupture, are distributed along a broad NNE-SSW structure with shallow seismicity (Fig. 4a-b) and have a total length of approximately 20 km. This rupture length is confirmed by inverting synthetic aperture radar (SAR) data (Lin et al., 2015; Kobayashi et al., 2018). The rupture length is likely greater than the expected for a M_w 6–6.2 (we estimated 8 km in total from the rupture directivity analysis). This may be due to, (1) the simple fault geometry that the code can provide and, (2) the larger fault dimensions of the aftershock cluster (compared to the primary slip surface) due to static-triggering of small faults beyond the borders of the main rupture.

The final best rupture model (purple arrows in Fig. 4a) provides a fault rupture direction of N60° with a total length of 8 km and a nearly pure bi-lateral propagation (e.g., equal predominant and secondary rupture lengths of 4 km) at an average rupture velocity of 0.9β (with β being the S-wave velocity). We note that the retrieved bi-lateral rupture mode and length match well the mainshock epicenter location and the early-time (3 h after MOT) spatial aftershock distribution. Moreover, the rupture orientation derived from the mainshock directivity analysis, points toward South-West and North-East which correspond well to the 1–3 km shallow and 4–6 km deep, high-slip mainshock fault patch, respectively (Kobayashi et al., 2018, see Fig. S15 in SM).

During the first phase of aftershocks, the seismicity deepens moving toward north-east (Fig. 4a-b and Fig. 5a,e,i,m), reaching up to 8–9 km depth in the northernmost sector (Fig. 5a). Moreover, the northern segment is more populated with aftershocks and characterized by a small cluster activated by the major aftershock of M_{JMA} 4.4 at 4 km of depth during the first hour after the MOT (green star in Fig. 4a-b and Fig. 5a). Using the seismicity belonging to this cluster in the entire time period (red dots in Fig. 4f and seismicity between 2 and 5 km of depth in Fig. 3 and 5d), we calculated the composite focal mechanism (cluster B in the Table S1 and Fig. S7) and found a strike of 47°, dip 61°, consistent with the fault segment associated with the mainshock rupture and the distribution of seismicity (Fig. 4f and Fig. 5a-d).

The south-western seismicity delineates a single fault plane that is co-located with the OTNF structure (Fig. 4a-b and Fig. 5a-d; Panayotopoulos et al., 2016). In detail, the aftershocks delineate a fault segment in the south of 8 km length with a strike of around 20° (Fig. 4a) and mainly up to 4 km of depth indicating that the mainshock ruptured upward (Fig. 5i). In previous work on the sequence (Panayotopoulos et al., 2016; Ando et al., 2017) there is almost no seismicity in the upper two kilometers of the crust in the southernmost section compared to the locations obtained in this paper (section A-A' on Fig. 4a-b and Fig. 5m). This discrepancy mostly reflects the difference of the catalog and on the use of the 3D velocity model that accounts for the strong lateral variation in velocity across the area characterized by two different domains (INZ and NFM in Fig. 1) side by side. We can note that the result is consistent with slip distribution on the fault estimated by Kobayashi et al., 2018. Indeed, the seismicity in the first 2 km depth in the southernmost area of the sequence (Fig. 4a-b and Fig. 5m) is located around the shallow high-slip patch of the mainshock (Fig. S15 in SM).

By considering the seismicity clustered around the mainshock location (magenta dots in Fig. 4f), we calculated the composite focal mechanism (cluster A in the Table S1 and Fig. S6) and found a fault plane with a strike of 20° and east-dipping at 55° which is consistent with the distribution in plane (Fig. 4f) and in depth (Fig. 3 and 5l) of clustered seismicity and with the mainshock CMT solution estimated by the NIED using Full Range Seismograph Network of Japan (F-net) (National Research Institute for Earth Science and Disaster Prevention, 2014) (see Fig. 4a-b and Table S2). For the shallow seismicity at <2 km depth in the southernmost section A-A' (pink dots on Fig. 4f), we calculated the composite focal mechanism (cluster C in the Table S1 and Fig. S8) and found a fault plane with a strike of 20° and east-dipping of 50° which is consistent with the distribution of seismicity along the fault segment in the southern area.

We note that the clusters A-B-C show a sense of movement consistent with the orientation of the regional stress field. Clusters A and C show a clear reverse sense of movement, while cluster B shows a right lateral strike-slip sense of shear, likely due to the rotation of the fault toward the east in the northern area.

4.2. Phase 2 / Deep aftershocks distribution in the northern area

Between 12 and 24 h after the MOT, in the northern area (i.e., section C-C'), a second major shock with M_{JMA} 4.4 occurred (green star in Fig. 4c and Fig. 5f) on a different fault segment. For the cluster associated with this major aftershock (black dots in Fig. 4f), we calculated the composite focal mechanism (cluster D in the Table S1 and Fig. S9) to produce a fault plane striking at 210° and west-dipping 60°, consistent with the seismicity depth distribution (Fig. 5f) and with the major aftershock CMT solution estimated by NIED using F-net (National Research Institute for Earth Science and Disaster Prevention, 2014) (Table S2). In the northernmost section D-D', a significant increase of events is observed in the deep part (up to 8 km depth) of the northern sector (Fig. 5b).

After 24 h from the MOT, we observed a significant increase of the number of events in the deeper part of the fault surface, between 6 and

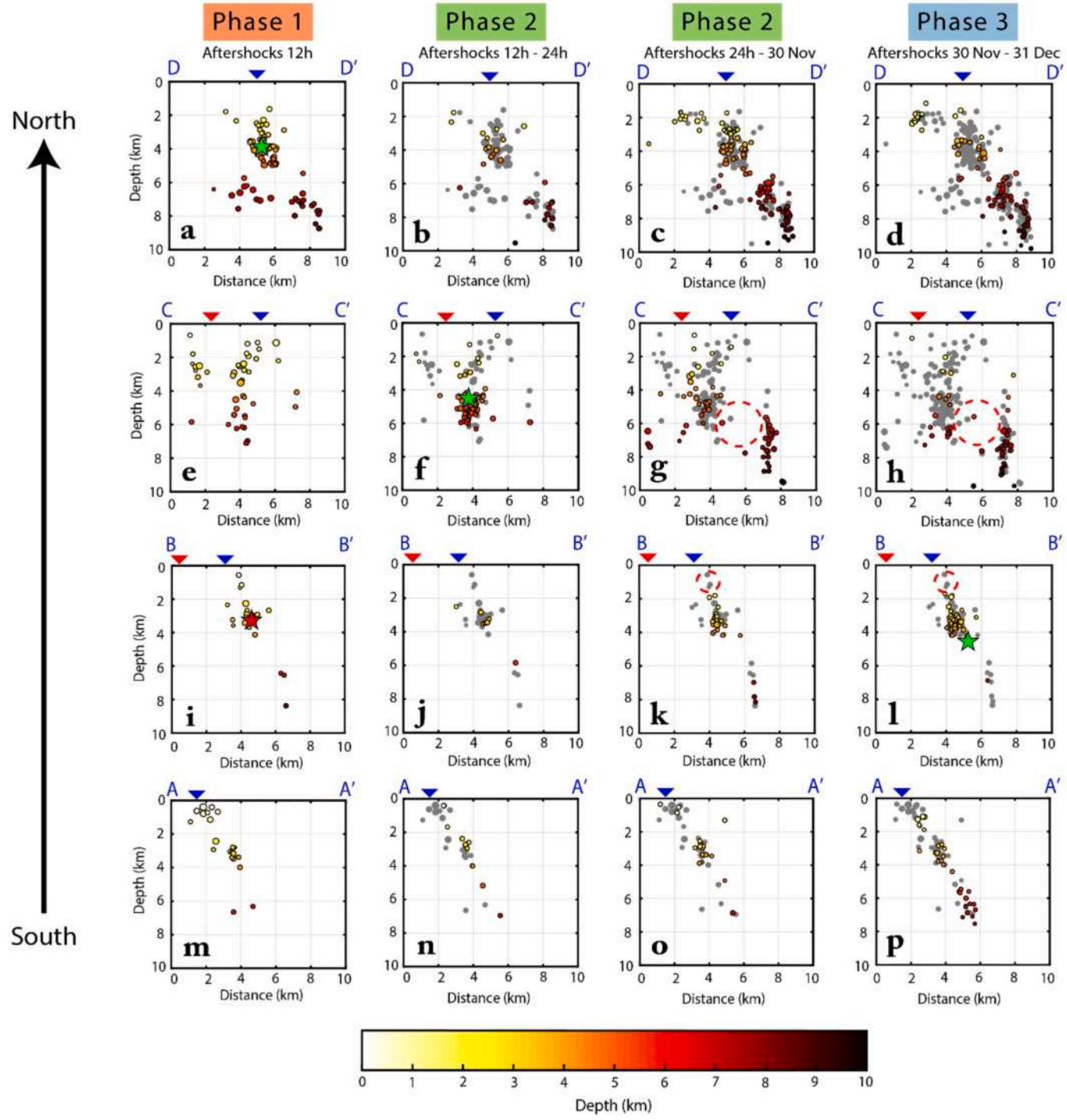

Fig. 5. Cross-sections of the aftershock sequence perpendicular to fault strike at different time periods (i.e., phases 1, 2, &3) after the mainshock. Red star denotes the mainshocks and the green stars correspond to the major aftershock with a $M_{JMA} \geq 4$. Circles denote aftershocks and sizes scale with magnitudes. Gray circles correspond to the aftershocks which occurred before the time interval presented. Colored aftershock circles indicate depth of the aftershocks (see colour bar for depth scale). Red dash contours indicate the positions of the high-slip patches from the model estimated by Kobayashi et al. (2018). (For interpretation of the references to colour in this figure legend, the reader is referred to the web version of this article.)

10 km of depth, starting from the northernmost section D-D′ up to the section B-B′ in the area of the mainshock (Fig. 4d and Fig. 5c,g). However, it's not easy to define the activation time of the deep seismicity in the southern area. In section D-D′ (Fig. 5c), we distinguish two separate clusters, one between 6 and 8 km depth (blue dots in Fig. 4f) and the second deeper cluster, between 7 and 10 km (green dots in Fig. 4f). We calculated clusters the composite focal mechanisms for each of the clusters and found their spatial distributions to be consistent with the strike and drip from CMT solution. The CMT solution of the cluster (cluster E in the Table S1 and Fig. S10) between 6 and 8 km of depth (blue dots in Fig. 4f) has a fault plane with a strike of 70° and southward dip of 80° and for cluster (cluster F in the Table S1 and Fig. S11) between 7 and 10 km (green dots in Fig. 4f) has a fault plane striking at 254° with a dip of 61° north. Moving toward the south-west, in the section C-C′ (Fig. 4d and Fig. 5g), a cluster with a near-vertical distribution is clearly observed. For this deeper cluster (cyan dots in Fig. 4f), we calculated a

composite focal mechanism (cluster G in the Table S1 and Fig. S12) with a strike of 206° and an eastward dip of 77°, which matches the seismicity distributions. Given the time delay of hours between these four clusters and the main rupture, we hypothesize that static stress transfer is the likely triggering mechanism for these aftershocks. Also in the same period, we can observe an increase of seismicity in the southernmost area (section A-A') between 2 and 4 km of depth (orange dots in Fig. 4f). The composite focal mechanism (cluster H in the Table S1 and Fig. S13) gives a fault plane with a strike of 20° and a dip of 80° to the east.

We can observe the variability of the rupture behavior of the clusters during this phase with the clusters D, E, and F which are showing a right lateral strike-slip sense of movement, the cluster G is showing a normal movement, and the cluster H is showing a left lateral strike-slip sense of movement.

In previous studies, the authors associated the deep seismicity in the northern area (Fig. 4c-d and Fig. 5b-c-f-g) to the extension of the mainshock fault at depth (Panayotopoulos et al., 2016; Ando et al., 2017). The small-scale complexity that we can reveal by considering high precision locations obtained refining the absolute picks, allowed us to identify and geometrically characterize these clusters. For each of these clusters the estimated dominant focal mechanisms show sub-vertical planes consistent with the seismicity delineated fault. Our analysis suggests that the deep seismicity in the northern area did not occur on the same fault plane as the mainshock but was part of a wider fault surface comprising sub-parallel segments.

4.3. Phase 3 / Deep aftershocks distribution in the southern area

One week after the MOT, the southernmost area (section A-A') was characterized by an increase of seismicity to a depth of 5 km (Fig. 4e and Fig. 5p). We calculated the composite focal mechanism (cluster I in the Table S1 and Fig. S14) and found a fault plane solution with a strike of 16° and a dip of 77° to the east for the deep seismicity in the southern area (yellow dots in Fig. 4f).

By identifying the small-scale complexity of the southernmost area at section A-A', we distinguish the higher dipping structures of two deeper clusters (H and I) with respect to the shallower structures (cluster C on Fig. 4f and Fig. S8). The deeper clusters H and I show a left lateral strike-slip sense of movement, while the cluster C, activated during the mainshock rupture phase, shows reverse kinematics. The gaps in aftershocks at 6 km depth in the northern area (red dashed contoured area in section C-C′, Fig. 5h) and up to 2 km above the mainshock cluster (red dashed contoured area in section B-B′, Fig. 5l) are well correlated with a high slip patch of the mainshock rupture (Kobayashi et al., 2018; see Fig. S15 in SM).

The shallower seismicity, $\leq$ 6 km depth, shows several relatively high magnitude shocks, followed by a power-decaying number of events with time from the mainshock (see Fig. 3 and S16 in SM). On the other hand, the deeper volume seems to have not been activated by major aftershocks and the temporal distribution of seismicity is almost constant in time (see Fig. S16 in SM). Thus, we can observe a different behavior in terms of seismicity time occurrence between the shallow and deep part of the fault surface and between the northern and southern areas. This different behavior of cluster-events with time within the same seismic sequence has been observed in other seismic regions worldwide and associated with different triggering mechanisms, static-stress transfer or pore-fluid induced effect (De Barros et al., 2019). Furthermore, this could also arise from the fact that some of the fault segments from the deep portion of the fault surface are very steep, and therefore may not be optimally oriented to be (re)activated. However, further and more quantitative investigations are required to explain the different behavior of the cluster-events.

4.4. Segmented fault surface

As previously mentioned, the fault system responsible for the Nagano earthquake sequence is an inherited extensional fault which is currently being reactivated with primarily reverse kinematics in response to the inversion of the NFM basin. Although some characteristics of the original, extensional fault system such as the dip or strike of individual fault segments may have been during fault inversion, the bulk 3D geometry (e.g., degree of fault segmentation, types of linkage between adjacent fault segments) is likely to have been preserved through the episode of fault reactivation and inversion.

In describing and interpreting the 3D structure of the fault surface, we adopt geometrical templates and associated terminologies that have been used for extensional faults. It is well-known that extensional faults are seldom individual planar surfaces in 3D, and most often comprised of multiple fault segments (Walsh and Watterson, 1989; Childs et al., 1996, 2009; Peacock, 2002; Marchal et al., 2003; Walsh et al., 2003; Kristensen et al., 2008; Delogkos et al., 2017; Camanni et al., 2021, 2023b; Roche et al., 2021). An important notion to be introduced here is that of "relay zone", defined as the volume of rocks between two adjacent fault segments, whose deformation facilitates the transfer of displacement from one fault segment to another (Larsen, 1988; Peacock and Sanderson, 1991, 1994; Childs et al., 1995; Huggins et al., 1995; Camanni et al., 2019, 2023a, 2023b; Delogkos et al., 2020; Nicol et al., 2020; Roche et al., 2020, 2021). In this work we are not concerned with the exact mechanism for transferring displacement across relay zones, but rather are focused on their 3D geometry. Therefore, in this section, we will first describe the 3D nature of the studied fault surface, and we then compare it with other templates of 3D segmented normal fault surfaces described in the literature.

The southernmost fault segment is made up of a single, planar, east-dipping surface (segment A in Fig. 7, section B-B′ in Fig. 6) which, in the south, splays into three, subordinate segments juxtaposed across two relay zones with a sub-horizontal axis (segments C-I-H in Fig. 7, section A-A' in Fig. 6). It is worth noting here that, in cross-section (panel b in Fig. 6), the envelopes of these three segments have a dip angle which is steeper than that of segment A (Fig. 6–7).

The northernmost fault segment is geometrically more complex than the southern area (Fig. 6–7). Overall, it comprises two subordinate fault segments vertically juxtaposed across a relay zone, with a sub-horizontal relay axis; an antithetic fault (i.e., more prominently west-dipping) is associated with this relay zone (segment D in Fig. 7, section C-C′ in Fig. 6). The upper segment (segment B in Fig. 6–7), is an individual east-dipping surface, while the lower segment is a sub-vertical to steeply west-dipping surface (segment G in Fig. 6–7). The segment G splays into two minor segments (segments E and F in Fig. 6–7) toward the north which are juxtaposed across a sub-horizontal relay zone (section D-D′ in Fig. 6).

5. Discussion

5.1. 3D structure of the seismological-derived fault surface

The seismological-derived 3D structure of the fault surface has several geometrical characteristics similar to the 3D structure of normal faults from fault mapping of higher resolution datasets such as field and 3D seismic reflection (e.g., Marchal et al., 2003; Kristensen et al., 2008; Tvedt et al., 2013; Worthington and Walsh, 2017; Freitag et al., 2017; Lăpădat et al., 2017; Camanni et al., 2019; Roche et al., 2020, 2021). Direct comparison between datasets is viable since the segmentation of the fault studied here is interpreted to be inherited from an extensional fault. In particular, recent work (e.g., Camanni et al., 2019; Roche et al., 2021) show that, overall, relay zones on normal faults are mostly either sub-horizontal (i.e., neutral relay zones) or sub-vertical (i.e., dip relay zones); a characteristic in common with the fault zone studied here. Similarly, in circumstances where normal faults are vertically segmented, it has been shown that the individual fault segments have a sense of stepping which gives rise to mostly contractional rather than extensional strains in the relay zones (e.g., Camanni et al., 2019). This

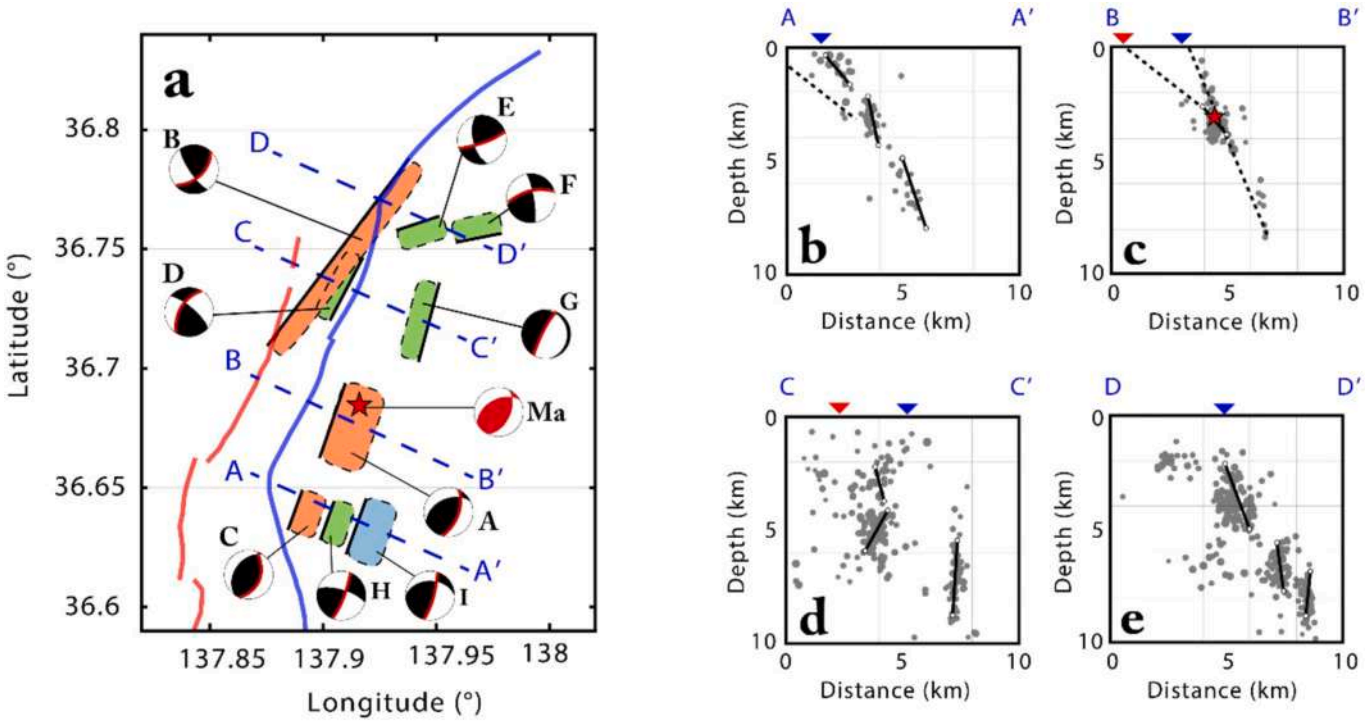

Fig. 6. Map (a) and cross-section (b-e) views of the main fault segments identified in this study. The colour of the segment is following the 3 phases discussed in this study (orange: first phase; green: second phase; blue: third phase). The index letters of each composite focal mechanism are referred in the Table S1 in SM. The red and blues lines on the map correspond to the fault traces at the surface of the Kamishiro fault and the Otari-Nakayama fault respectively. The red and blue triangles on the sections correspond to the position of the fault trace at the surface of the Kamishiro fault and the Otari–Nakayama fault respectively. (For interpretation of the references to colour in this figure legend, the reader is referred to the web version of this article.)

appears to also be valid for the fault zone studied here, where the horizontally segmented faults have relay zones with a contractional geometrical configuration (see, e.g., relay zones between segments C-I-H, and relay zones between segments B-*E*—F). Finally, it is worth mentioning here that the resolution of the hypocenter data used in this study does not allow us to define whether segments are connected. However, for the sake of clarity, in Fig. 6–7 segments are drawn as physically disconnected.

5.2. Implications of 4D analysis on stress triggering models and seismic hazard

Fault segments, during an earthquake, interact through stress transfer, and understanding these interactions is crucial for predicting how seismic events may trigger activity on adjacent segments. Reconstructing faults in 3D offers a more detailed view of these interactions, improving stress transfer models and predictions of fault behavior. After a rupture, stress redistributes to neighboring segments that could influence their ruptures depending on the geometry and the orientation (Stein, 1999). Coulomb stress change models are especially sensitive to fault geometry, with variations in orientation and segmentation affecting stress redistribution (King et al., 1994; Stein, 1999; Toda et al., 2005). Simplified models may miss key details, such as fault bends, stepovers, or branching structures (King et al., 1994). Fault inversion models that incorporate detailed 3D reconstructions can better capture these spatial variations, leading to more accurate predictions of segment behavior during seismic events (Noda and Lapusta, 2013).

In our complex fault surface model based on the spatial distribution of earthquakes together with the composite focal mechanisms of significant clusters, we found that the fault segments associated with the aftershocks in the different phases of the Nagano sequence are located around the dominant slip path of the mainshock (Fig. 8). The volume around the dominant slip path can be associated with the regions where Coulomb stress increases, as these areas experience the highest stress transfer following a rupture (King and Cocco, 2001; Toda et al., 2011; Ross et al., 2017; Hardebeck, 2021; Gong et al., 2024). The final 3D segmented model is then consistent with these observations.

Moreover, the highly segmented nature of the surface during the Nagano earthquake sequence suggests that the rupture process could be more of a cascading phenomenon than a single continuous rupture front propagating along a fault. Along the reconstructed segmented fault surface, we found a high variability of P- and T-axes direction especially with depth (Fig. 7). The analysis of the temporal sequence of activation of the 3D segments (Fig. 8) within the time windows previously described, provide insights on the 4D evolution of rupture activated during the 2014 Nagano earthquake sequence. We can note the difference of the rupture kinematics of the segments among the fault surface of the later phases with respect to the ones of the first phase. This variation of the rupture kinematics can be explained by (i) a strong variation of the fault geometry with respect to the orientation of the regional stress field and (ii) the variation of the strain among the fault surface in the days/weeks after stress release due to the mainshock rupture. These results suggest that the initial structure of the segmented fault surface, that ruptured during the sequence, has a key control not only on earthquake clustering but also on the seismicity evolution, including the segments activation and their kinematics into the three rapture phases.

The proposed framework for reconstructing the fault surface involved in the Mw 6.2, 2014 Nagano aftershock sequence that integer the discontinuities and the strain variability along the fault surface will lead to a more reliable evaluation of slip distribution of the main rupture (Cesca et al., 2017), stress transfer mechanisms to neighboring segments, linking behaviors among adjacent segments (Hodge et al., 2018), and identification of segments that are likely to rupture next, providing valuable information for surface faulting hazard assessments (Pratt et al., 1998; Improta and Bruno, 2007; Kaiser et al., 2011; Bruno, 2023;

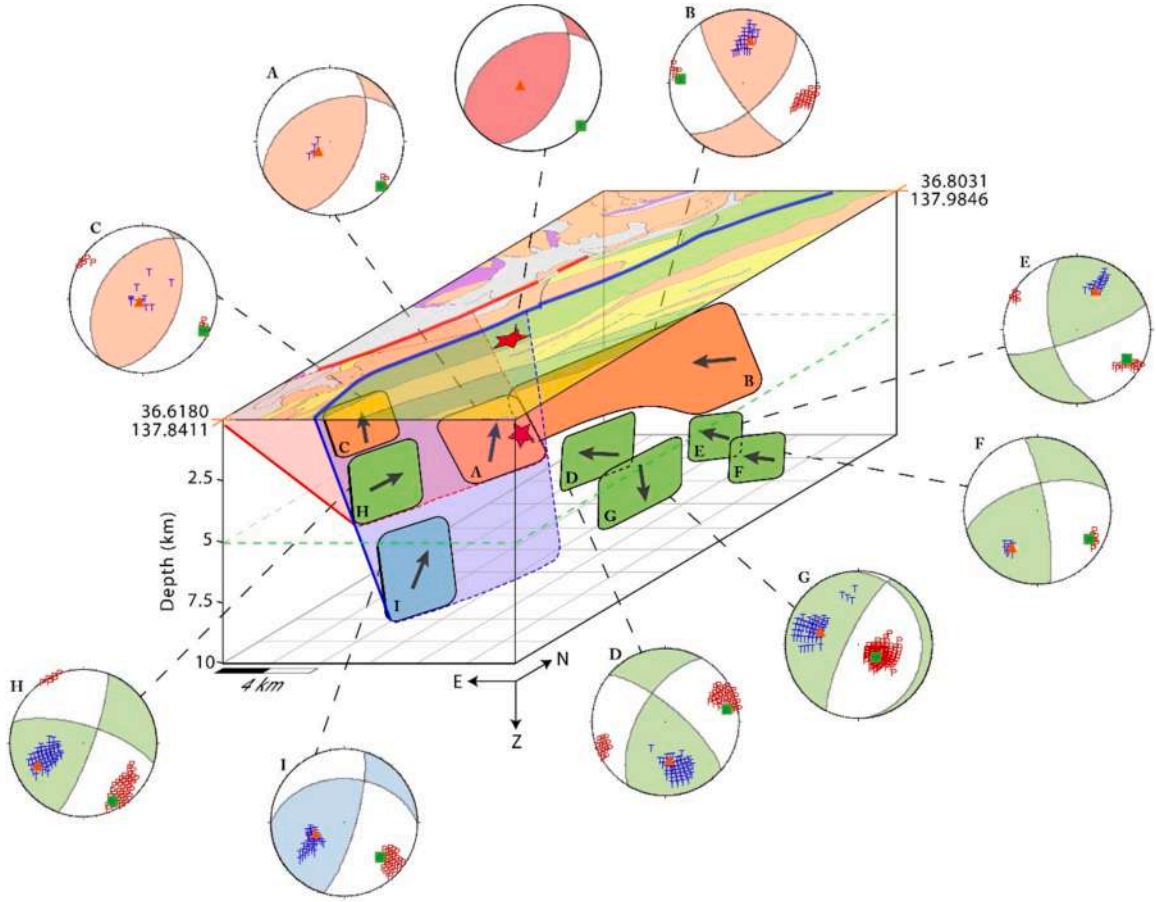

Fig. 7. 3D model of the studied segmented fault surface and geological map of the study area (colors in the map are as in Fig. 1). The colour of the segment and the focal mechanism is following the 3 phases discussed in this study (orange: first phase; green: second phase; blue: third phase). The gray arrows on the segments represent the movement on the fault with respect to the estimated focal mechanisms. The index letters of each fault segment are referred to Table S1 in SM. The red and blues lines on the map correspond to the fault traces at the surface of the Kamishiro fault and the Otari–Nakayama fault respectively. The red and blue surfaces at depth correspond to the position of the fault plane of the Kamishiro fault and the Otari–Nakayama fault respectively. The orange triangle and the green square on the focal mechanisms represent the projection of the T-axis and P-axis, respectively. (For interpretation of the references to colour in this figure legend, the reader is referred to the web version of this article.)

Maraio et al., 2023).

Several complex ruptures have shown that the fault surface discontinuities have to be considered for reliable surface faulting scenarios (2010 Mw 7.1 Canterbury, Gledhill et al., 2011; 2012 Mw 8.6 Sumatra, Satriano et al., 2012; 2016 Mw 7.8 Kaikoura, Cesca et al., 2017; 2016 Mw 6.5 central Italy, Scognamiglio et al., 2018). Segments may rupture independently in smaller size but more frequent events, or rupture together in larger size with less frequent earthquakes, with stronger ground motions and higher seismic hazards. Segment interaction depends on fault discontinuities at a scale of a few kilometers length, as fault bends or stepovers (Howell et al., 2024). In terms of hazard, on the short-term (e.g., 500 years), fault models in which the ruptures are confined to individual fault segments (segmented model) have slightly higher hazard with respect to fault model in which ruptures could involve different segments (named multi-fault) because the seismic moment is accommodated by frequent moderate earthquakes (Valentini et al., 2020; Howell et al., 2024). But, on the long-term hazard assessments, simulating the segment interaction with a reliable model (multi-fault), allows to include in the hazard scenarios the less probable, but more destructive, large magnitude ($M_w > 6$) event (Howell et al., 2024) which considerably raises the seismic hazard. Indeed, over longer time periods (e.g., 2500 years), the likelihood of a larger multi-segment rupture becomes more relevant, as such large events tend to have longer recurrence intervals (Wesnousky, 2006; Field and Page, 2013). In our case, detailing the geometry and kinematics of the complex fault segments, whereas the different phases of rupture following the mainshock, would enhance the surface faulting hazard evaluation of the ISTL at local scale over long time periods.

Finally, for near-term (e.g., < 50 yrs) hazard scenario assessment, the high precision analysis of aftershock spatio-temporal evolution for a large time span after the mainshock (one month), reconstructing also the involved fault segments, is crucial. The aftershock occurrence can affect the near-term seismic hazard through, principally, two mechanisms, the stress redistribution and the fault weakening. The stress transfer can either increase or decrease the likelihood of future seismic events on nearby faults (depending on the fault geometry and the orientation of the stress field), while the fault weakening make the fault more susceptible to future ruptures by increasing the probability of significant seismic activity in the near term (Scholz, 2010). These effects are particularly significant in regions with complex fault systems, where interactions between fault segments can amplify seismic risk over a short time frame (Scholz, 2010; Miller, 2020).

6. Conclusions

With the aim to reconstruct the 4D multi-segmented rupture history of the 2014 M_w 6.2 Nagano sequence, by relocating about 2500 aftershocks to reconstruct an enhanced catalog with high-resolution locations (e.g. 100–200 m). We increased the three-month JMA seismic catalog of around the mainshock by around 10 %. Then, we used a new

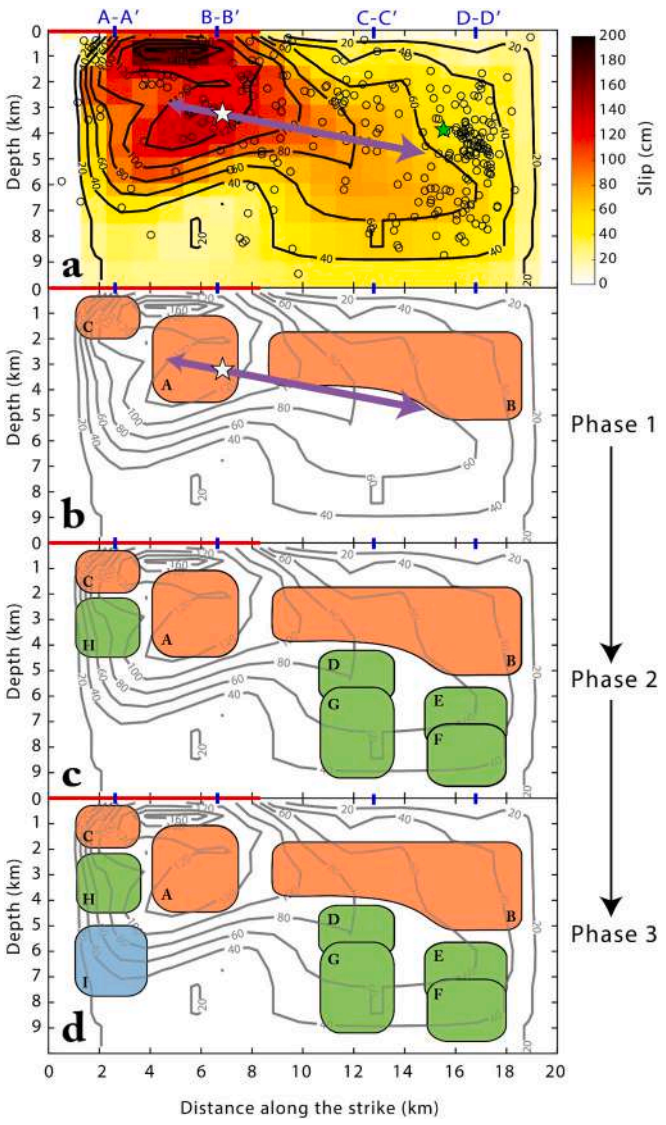

Fig. 8. Fault strike-projection views of (a) the aftershock seismicity over the entire time period on the slip model obtained by Kobayashi et al., 2018 and (b-e) the 4D seismicity evolution of the Nagano earthquake sequence in the 3 phases described in this study (orange, phase 1; green, phase 2; blue, phase 3). The colour of the segment denotes the 3 phases. The index letters of each fault segment are referred to in Table S1 of the SM. Black circles indicate the aftershock location. White star indicates the M_w 6.2 mainshock location. The gray lines indicate the contour of the slip along the fault. The purple arrows indicate the rupture directivity and the rupture mode of the mainshock. The red line indicates the position of the surface rupture. (For interpretation of the references to colour in this figure legend, the reader is referred to the web version of this article.)

method for the refinement of automatic picks that includes; 1) the construction of a family of co-located events with high cross-correlation of waveforms at the same station; 2) the construction of a reference trace for each family through a weighted stack of waveforms on which measure a reference automatic pick; 3) the use of a reference pick to adjust the other picks of waveforms in the family. Each pick is associated with a weight based on the SNR ratio around the refined pick. This procedure is crucial, together with the use of reliable 3D velocity models, to obtain accurate depth estimations of events. The refined picks were inverted by a tomographic approach to obtain 3D P- and S-wave velocity models. We obtained the final location catalog by using the double-difference method and 3D velocity models (P and S-phase) optimized for the study area.

By using these methods, the highly accurate relocation allowed us to unravel the 3D small-scale geometric complexities of the fault surface by analyzing the spatial distribution of the aftershocks with unprecedented detail. The early aftershock distribution and the strong motion data confirm the bilateral propagation of the mainshock rupture consistent with the distribution of aftershocks in the first 3 h after the mainshock. By following the aftershock evolution in time, a complex cascading rupture phenomena can be unraveled with rupture of 9 different fault segments well constrained in terms of their geometry, timing in 3D and composite focal mechanisms. The temporal evolution of fault rupture into 3 phases involved first the shallow northern and southern areas of the fault surface, then the deeper northern portion of the system and finally the deeper and the shallower part of the southern area. Among the different fault segments, we observe different kinematic behavior for the segments, which can be explained by ruptures variations in the fault geometry together with temporal and spatial changes in the stress field in the days/weeks after the mainshock rupture. This application to reconstruct the complexity of the fault surface can be used both for guiding the fault mapping at depth in active fault areas and better understand the earthquake rupture.

The 4D fault reconstruction enhances stress transfer models and seismic predictions. In the Nagano earthquake sequence, aftershocks were concentrated around the main slip path, associated with the regions where Coulomb stress increases. The complex fault geometry influences seismicity evolution and short- and long-term seismic hazard, with segments potentially rupturing separately or together, leading to larger magnitude earthquakes.

Data & software availability statement

The continuous seismic records (Hi-net data) analyzed in this paper are available via doi:10.17598/NIED.0003. The strong motion data (KiK-net data) of the mainshock records are available from the National Research Institute of Earth Science and Disaster Resilience (https://www.doi.org/10.17598/NIED.0004). The absolute locations were processed by using the code NonLinLoc (http://www.alomax.net/nlloc). The composite focal mechanisms were computed using the code FPFIT (available on USGS via https://www.usgs.gov/software/fpfit-fpplot-and-fppage).

CRediT authorship contribution statement

Titouan Muzellec: Writing – review & editing, Writing – original draft, Visualization, Validation, Software, Resources, Methodology, Investigation, Formal analysis, Data curation, Conceptualization. **Grazia De Landro:** Writing – review & editing, Writing – original draft, Visualization, Validation, Supervision, Software, Resources, Methodology, Investigation, Formal analysis, Conceptualization. **Giovanni Camanni:** Writing – review & editing, Writing – original draft, Visualization, Validation, Investigation, Formal analysis, Conceptualization. **Guido Maria Adinolfi:** Writing – original draft, Validation, Software. **Aldo Zollo:** Writing – review & editing, Writing – original draft, Validation, Supervision, Project administration, Methodology, Funding acquisition, Formal analysis, Conceptualization.

Declaration of competing interest

The authors declare that they have no known competing financial interests or personal relationships that could have appeared to influence the work reported in this paper.

Data availability

Data will be made available on request.

Acknowledgments

The authors thank Vincenzo Convertito (INGV) for providing the code for rupture direction analysis and the support for its use. The authors acknowledge financial support from the Project TRHAM - "Relation Between 3d Thermo-Rheological Model And Seismic Hazard For The Risk Mitigation In The Urban Areas Of Southern Italy" funded by the European Union - Next Generation EU, Mission 4, Component 2 - CUP B53D23033710001 - Grant Number P2022P37SN. The authors acknowledge financial support from the Project FRACTURES - "Multi-scale study of seismogenic processes in Campania-Lucania Apennines using machine learning algorithms and multiparametric observations" funded by the European Union - Next Generation EU, Mission 4, Component 2 - CUP B53D23006980006 - Grant Number 2022BEKFN2. The work of AZ was supported in part by Project "PE0000005–RETURN-SPOKE 3-CUP UNINA: E63C220002000002". We would like to thank the Editor, Andy Nicol, and the anonymous reviewer for their comments and suggestions that allowed us to improve the manuscript.

Appendix A. Supplementary data

Supplementary data to this article can be found online at https://doi.org/10.1016/j.tecto.2025.230641.

References

Adinolfi, G.M., Picozzi, M., Cesca, S., Heimann, S., Zollo, A., 2020. An application of coherence-based method for earthquake detection and microseismic monitoring (Irpinia fault system, Southern Italy). J. Seismol. 24, 979–989.
Adinolfi, G.M., De Matteis, R., De Nardis, R., Zollo, A., 2022. A functional tool to explore the reliability of micro-earthquake focal mechanism solutions for seismotectonic purposes. Solid Earth 13 (1), 65–83.
Adinolfi, G.M., De Landro, G., Picozzi, M., Carotenuto, F., Caruso, A., Nazeri, S., Piantanida, M., 2023. Comprehensive study of micro-seismicity by using an automatic monitoring platform. Front. Earth Sci. 11, 1073684.
Aki, K., Richards, P.G., 2002. Quantitative seismology.
Amoroso, O., Napolitano, F., Hersir, G.P., Agustsdottir, T., Convertito, V., De Matteis, R., Capuano, P., 2022. 3D seismic imaging of the Nesjavellir geothermal field, SW-Iceland. Front. Earth Sci. 10, 994280.
Ando, R., Imanishi, K., Panayotopoulos, Y., Kobayashi, T., 2017. Dynamic rupture propagation on geometrically complex fault with along-strike variation of fault maturity: insights from the 2014 Northern Nagano earthquake. Earth Planets Space 69 (1), 1–13.
Asano, Y., Saito, T., Ito, Y., Shiomi, K., Hirose, H., Matsumoto, T., Hiro, S., Sekiguchi, S., 2011. Spatial distribution and focal mechanisms of aftershocks of the 2011 off the Pacific coast of Tohoku Earthquake. Earth Planets Space 63 (7), 669–673.
Bailey, I.W., Ben-Zion, Y., Becker, T.W., Holschneider, M., 2010. Quantifying focal mechanism heterogeneity for fault zones in central and southern California. Geophys. J. Int. 183 (1), 433–450.
Baillard, C., Crawford, W.C., Ballu, V., Hibert, C., Mangeney, A., 2014. An automatic kurtosis-based P-and S-phase picker designed for local seismic networks. Bull. Seismol. Soc. Am. 104 (1), 394–409.
Barka, A.A., Kadinsky-Cade, K., 1988. Strike-slip fault geometry in Turkey and its influence on earthquake activity. Tectonics 7 (3), 663–684.
Bruno, P.P.G., 2023. Seismic Exploration Methods for Structural Studies and for active Fault Characterization: a Review. Appl. Sci. 13 (16), 9473.
Buttinelli, M., Petracchini, L., Maesano, F.E., D'Ambrogi, C., Scrocca, D., Marino, M., Capotorti, F., Bigi, S., Cavinato, G.P., Mariucci, M.T., Montone, P., 2021. The impact of structural complexity, fault segmentation, and reactivation on seismotectonics: Constraints from the upper crust of the 2016–2017 Central Italy seismic sequence area. Tectonophysics 810, 228861.
Camanni, G., Brown, D., Alvarez-Marron, J., Wu, Y.M., Chen, H.A., 2014. The Shuilikeng fault in the Central Taiwan mountain belt. J. Geol. Soc. Lond. 171 (1), 117–130.
Camanni, G., Roche, V., Childs, C., Manzocchi, T., Walsh, J., Conneally, J., Delogkos, E., 2019. The three-dimensional geometry of relay zones within segmented normal faults. J. Struct. Geol. 129, 103895.
Camanni, G., Vinci, F., Tavani, S., Ferrandino, V., Mazzoli, S., Corradetti, A., Iannace, A., 2021. Fracture density variations within a reservoir-scale normal fault zone: a case study from shallow-water carbonates of southern Italy. J. Struct. Geol. 151, 104432.
Camanni, G., Childs, C., Delogkos, E., Roche, V., Manzocchi, T., Walsh, J., 2023a. The role of antithetic faults in transferring displacement across contractional relay zones on normal faults. J. Struct. Geol. 168, 104827.
Camanni, G., Freda, G., Delogkos, E., Nicol, A., Childs, C., 2023b. 3D geometry and displacement transfer of an oblique relay zone on outcropping normal faults. J. Struct. Geol. 177, 105001.
Cesca, S., Zhang, Y., Mouslopoulou, V., Wang, R., Saul, J., Savage, M., Dahm, T., 2017. Complex rupture process of the Mw 7.8, 2016, Kaikoura earthquake, New Zealand, and its aftershock sequence. Earth Planet. Sci. Lett. 478, 110–120.
Childs, C., Watterson, J., Walsh, J.J., 1995. Fault overlap zones within developing normal fault systems. J. Geol. Soc. Lond. 152 (3), 535–549.
Childs, C., Nicol, A., Walsh, J.J., Watterson, J., 1996. Growth of vertically segmented normal faults. J. Struct. Geol. 18, 1389–1397.
Childs, C., Manzocchi, T., Walsh, J.J., Bonson, C.G., Nicol, A., Schöpfer, M.P., 2009. A geometric model of fault zone and fault rock thickness variations. J. Struct. Geol. 31 (2), 117–127.
Cockerham, R.S., Eaton, J.P., 1987. The earthquake and its aftershocks, April 24 through September 30, 1984. The Morgan Hill, California. Earthquake of April 24 (1984), 15–28.
Collanega, L., Siuda, K., Jackson, C.A.L., Bell, R.E., Coleman, A.J., Lenhart, A., Breda, A., 2019. Normal fault growth influenced by basement fabrics: the importance of preferential nucleation from pre-existing structures. Basin Res. 31 (4), 659–687.
Convertito, V., Caccavale, M., De Matteis, R., Emolo, A., Wald, D., Zollo, A., 2012. Fault extent estimation for near-real-time ground-shaking map computation purposes. Bull. Seismol. Soc. Am. 102 (2), 661–679.
De Barros, L., Baques, M., Godano, M., Helmstetter, A., Deschamps, A., Larroque, C., Courboulex, F., 2019. Fluid-induced swarms and coseismic stress transfer: a dual process highlighted in the aftershock sequence of the 7 April 2014 earthquake (Ml 4.8, Ubaye, France). J. Geophys. Res. Solid Earth 124 (4), 3918–3932.
De Landro, G., Amoroso, O., Russo, G., Zollo, A., 2020. 4d travel-time tomography as a tool for tracking fluid-driven medium changes in offshore oil–gas exploitation areas. Energies 13 (22), 5878.
De Landro, G., Amoroso, O., Russo, G., D'Agostino, N., Esposito, R., Emolo, A., Zollo, A., 2022. Decade-long monitoring of seismic velocity changes at the Irpinia fault system (southern Italy) reveals pore pressure pulsations. Sci. Rep. 12 (1), 1247.
Delogkos, E., Manzocchi, T., Childs, C., Sachanidis, C., Barbas, T., Schöpfer, M.P., Walsh, J.J., 2017. Throw partitioning across normal fault zones in the Ptolemais Basin, Greece. Geol. Soc. Lond. Spec. Publ. 439 (1), 333–353.
Delogkos, E., Manzocchi, T., Childs, C., Camanni, G., Roche, V., 2020. The 3D structure of a normal fault from multiple outcrop observations. J. Struct. Geol. 136, 104009.
Deng, H., McClay, K., Bilal, A., 2020. 3D structure and evolution of an extensional fault network of the eastern Dampier Sub-basin, North West Shelf of Australia. J. Struct. Geol. 132, 103972.
Field, E.H., Page, W.D., 2013. Fault segment boundaries and multi-segment ruptures: Implications for probabilistic seismic hazard analysis (PSHA). Seismol. Res. Lett. 84 (6), 1081–1090.
Freitag, U.A., Sanderson, D.J., Lonergan, L., Bevan, T.G., 2017. Comparison of upwards splaying and upwards merging segmented normal faults. J. Struct. Geol. 100, 1–11.
Gledhill, K., Ristau, J., Reyners, M., Fry, B., Holden, C., 2011. The darfield (Canterbury, New Zealand) Mw 7.1 earthquake of september 2010: a preliminary seismological report. Seismol. Res. Lett. 82 (3), 378–386.
Gong, W., Ye, L., Xu, S., Tan, Y., Chen, X., 2024. Rupture behaviors of the Southern Xianshuihe fault and seismicity around Mt. Gongga: Insights from the 2022 MW 6.6 Luding (China) earthquake sequence. Tectonophysics 230538.
Graymer, R.W., Langenheim, V.E., Simpson, R.W., Jachens, R.C., Ponce, D.A., 2007. Relatively simple through-going fault planes at large-earthquake depth may be concealed by the surface complexity of strike-slip faults. Geol. Soc. Lond. Spec. Publ. 290 (1), 189–201.
Hamling, I.J., Hreinsdóttir, S., Clark, K., Elliott, J., Liang, C., Fielding, E., Stirling, M., 2017. Complex multifault rupture during the 2016 M w 7.8 Kaikōura earthquake, New Zealand. Science 356 (6334), eaam7194.
Hardebeck, J.L., 2021. Spatiotemporal evolution of aftershock sequences from regional observations and rate-and-state friction modeling. J. Geophys. Res. Solid Earth 126 (1). https://doi.org/10.1029/2020JB020613 e2020JB020613.
Heimann, S., Kriegerowski, M., Isken, M., Cesca, S., Daout, S., Grigoli, F., Juretzek, C., Megies, T., Nooshiri, N., Steinberg, A., Sudhaus, H., Vasyura-Bathke, H., Willey, T., Dahm, T., 2017. Pyrocko - an Open-Source Seismology Toolbox and Library. GFZ Data Services, Potsdam. https://doi.org/10.5880/GFZ.2.1.2017.001.
Hirata, N., Ohmi, S., Sakai, S.I., Katsumata, K., Matsumoto, S., Takanami, T., Shimizu, H., 1996. Urgent joint observation of aftershocks of the 1995 Hyogo-ken Nanbu earthquake. J. Phys. Earth 44 (4), 317–328.
Hodge, M., Fagereng, Å., Biggs, J., 2018. The role of coseismic Coulomb stress changes in shaping the hard link between normal fault segments. J. Geophys. Res. Solid Earth 123, 797–814. https://doi.org/10.1002/2017JB014927.
Howell, A., Nicol, A., Bora, S., Gerstenberger, M., Van Dissen, R., Chamberlain, C., Shaw, B.E., 2024. Comparison of ground-shaking hazard for segmented versus multifault earthquake-rupture models in Aotearoa New Zealand. Seismol. Res. Lett. 95 (1), 186–200.
Hu, F., Zhang, Z., Chen, X., 2016. Investigation of earthquake jump distance for strike-slip step overs based on 3-D dynamic rupture simulations in an elastic half-space. J. Geophys. Res. Solid Earth 121 (2), 994–1006.
Huang, J., Deng, H., Mao, X., Chen, G., Yu, S., Liu, Z., 2023. 3D modeling of detachment faults in the Jiaodong gold province, eastern China: a Bayesian inference perspective and its exploration implications. Ore Geol. Rev. 154, 105307.
Huggins, P., Watterson, J., Walsh, J.J., Childs, C., 1995. Relay zone geometry and displacement transfer between normal faults recorded in coal-mine plans. J. Struct. Geol. 17 (12), 1741–1755.
Iacoletti, S., Cremen, G., Galasso, C., 2021. Advancements in multi-rupture time-dependent seismic hazard modeling, including fault interaction. Earth Sci. Rev. 220, 103650.
Imanishi, K., Uchide, T., 2017. Non-self-similar source property for microforeshocks of the 2014 Mw 6.2 Northern Nagano, Central Japan, earthquake. Geophys. Res. Lett. 44 (11), 5401–5410.

Improta, L., Bruno, P.P., 2007. Combining seismic reflection with multifold wide-aperture profiling: an effective strategy for high-resolution shallow imaging of active faults. Geophys. Res. Lett. 34 (20).
Japan Meteorological Agency, 2014. Monthly Report on Earthquakes and Volcanoes in Japan. November 2014. http://www.data.jma.go.jp/svd/eqev/data/gaikyo/monthly/201411/201411monthly.pdf.
Kaiser, A.E., Horstmeyer, H., Green, A.G., Campbell, F.M., Langridge, R.M., McClymont, A.F., 2011. Detailed images of the shallow Alpine Fault Zone, New Zealand, determined from narrow-azimuth 3D seismic reflection data. Geophysics 76 (1), B19–B32.
Kano, K., Kosaka, K., Murata, A., & Yanai, S. (1990). Intra-arc deformations with vertical rotation axes: the case of the pre-Middle Miocene terranes of Southwest Japan. Tectonophysics, 176(3–4), 333–354.
Kato, H., 1992. FOSSA MAGMA-A Masked Border Region Separating Southwest and Northeast Japan.
King, G., Cocco, M., 2001. Fault interaction by elastic stress changes: New clues from earthquake sequences. Adv. Geophys. 44, 1–38. https://doi.org/10.1016/S0065-2687(02)80006-0.
King, G., Nábělek, J., 1985. Role of fault bends in the initiation and termination of earthquake rupture. Science 228 (4702), 984–987.
King, G.C.P., Stein, R.S., Lin, J., 1994. Static stress changes and the triggering of earthquakes. Bull. Seismol. Soc. Am. 84 (3), 935–953.
Kobayashi, T., Morishita, Y., Yarai, H., 2018. SAR-revealed slip partitioning on a bending fault plane for the 2014 Northern Nagano earthquake at the northern Itoigawa–Shizuoka tectonic line. Tectonophysics 733, 85–99.
Kristensen, M.B., Childs, C.J., Korstgård, J.A., 2008. The 3D geometry of small-scale relay zones between normal faults in soft sediments. J. Struct. Geol. 30 (2), 257–272.
Lăpădat, A., Imber, J., Yielding, G., Iacopini, D., McCaffrey, K.J., Long, J.J., Jones, R.R., 2017. Occurrence and development of folding related to normal faulting within a mechanically heterogeneous sedimentary sequence: a case study from Inner Moray Firth, UK. Geol. Soc. Lond. Spec. Publ. 439, 373–394.
Larsen, P.H., 1988. Relay structures in a lower Permian basement-involved extension system, East Greenland. J. Struct. Geol. 10 (1), 3–8.
Latorre, D., Virieux, J., Monfret, T., Monteiller, V., Vanorio, T., Got, J.L., Lyon-Caen, H., 2004. A new seismic tomography of Aigion area (Gulf of Corinth, Greece) from the 1991 data set. Geophys. J. Int. 159 (3), 1013–1031.
Lin, A., Sano, M., Yan, B., Wang, M., 2015. Co-seismic surface ruptures produced by the 2014 Mw 6.2 Nagano earthquake, along the Itoigawa–Shizuoka tectonic line, central Japan. Tectonophysics 656, 142–153.
Lois, A., Sokos, E., Martakis, N., Paraskevopoulos, P., Tselentis, G.A., 2013. A new automatic S-onset detection technique: Application in local earthquake data. Geophysics 78 (1), KS1–KS11.
Lomax, A., Michelini, A., Curtis, A., Meyers, R.A., 2009. Earthquake location, direct, global-search methods. Encyclopedia of complexity and systems science 5, 2449–2473.
Manighetti, I., Campillo, M., Bouley, S., Cotton, F., 2007. Earthquake scaling, fault segmentation, and structural maturity. Earth Planet. Sci. Lett. 253 (3–4), 429–438.
Manighetti, I., Zigone, D., Campillo, M., Cotton, F., 2009. Self-similarity of the largest-scale segmentation of the faults: Implications for earthquake behavior. Earth Planet. Sci. Lett. 288 (3–4), 370–381.
Maraio, S., Villani, F., Bruno, P.P.G., Sapia, V., Improta, L., 2023. Active fault detection and characterization by ultrashallow seismic imaging: a case study from the 2016 Mw 6.5 Central Italy earthquake. Tectonophysics 850, 229733.
Marchal, D., Guiraud, M., Rives, T., 2003. Geometric and morphologic evolution of normal fault planes and traces from 2D to 4D data. J. Struct. Geol. 25 (1), 135–158.
Matsuta, N., Ikeda, Y., Sato, H., 2004. The slip-rate along the northern Itoigawa-Shizuoka tectonic line active fault system, Central Japan. Earth Planets Space 56 (12), 1323–1330.
Meng, H., Ben-Zion, Y., 2018. Detection of small earthquakes with dense array data: example from the San Jacinto fault zone, southern California. Geophys. J. Int. 212 (1), 442–457.
Miller, S.A., 2020. Complex fault interactions and triggering of earthquakes. Geophys. Res. Lett. 47 (12) e2020GL087926.
National Research Institute for Earth Science and Disaster Prevention, 2014. NIED seismic moment tensor catalogue. National Research Institute for Earth Science and Disaster Prevention available online from. http://www.fnet.bosai.go.jp/event/joho.php?LANG=en.
National Research Institute for Earth Science and Disaster Resilience, 2019. NIED K-NET, KiK-net, National Research Institute for Earth Science and Disaster Resilience. https://doi.org/10.17598/NIED.0004.
Nicol, A., Walsh, J., Childs, C., Manzocchi, T., 2020. The growth of faults. In: Understanding faults. Elsevier, pp. 221–255.
Noda, H., Lapusta, N., 2013. Stable creeping fault segments can become destructive as a result of dynamic weakening. Nature 493 (7433), 518–521. https://doi.org/10.1038/nature1170.
Okada, S., Ishimura, D., Niwa, Y., Toda, S., 2015. The First Surface-Rupturing Earthquake in 20 Years on a HERP Active Fault is Not Characteristic: The 2014 Mw 6.2 Nagano Event along the Northern Itoigawa–Shizuoka Tectonic Line. Seismol. Res. Lett. 86 (5), 1287–1300.
Otofuji, Y.I., Matsuda, T., Nohda, S., 1985. Paleomagnetic evidence for the Miocene counter-clockwise rotation of Northeast Japan—rifting process of the Japan Arc. Earth Planet. Sci. Lett. 75 (2–3), 265–277.
Palo, M., Picozzi, M., De Landro, G., Zollo, A., 2023. Microseismicity clustering and mechanic properties reveal fault segmentation in southern Italy. Tectonophysics 856, 229849.
Panayotopoulos, Y., Hirata, N., Sato, H., Kato, A., Imanishi, K., Kuwahara, Y., Cho, I., Takeda, T., Asano, Y., 2013. Investigating the role of the Itoigawa-Shizuoka tectonic line towards the evolution of the Northern Fossa Magna rift basin. Tectonophysics 615, 12–26.
Panayotopoulos, Y., Hirata, N., Hashima, A., Iwasaki, T., Sakai, S.I., Sato, H., 2016. Seismological evidence of an active footwall shortcut thrust in the Northern Itoigawa–Shizuoka Tectonic Line derived by the aftershock sequence of the 2014 M 6.7 Northern Nagano earthquake. Tectonophysics 679, 15–28.
Peacock, D. C. P. (2002). Propagation, interaction and linkage in normal fault systems. Earth Sci. Rev., 58(1–2), 121–142.
Peacock, D.C.P., Sanderson, D.J., 1991. Displacements, segment linkage and relay ramps in normal fault zones. J. Struct. Geol. 13 (6), 721–733.
Perrin, C., Manighetti, I., Ampuero, J.P., Cappa, F., Gaudemer, Y., 2016. Location of largest earthquake slip and fast rupture controlled by along-strike change in fault structural maturity due to fault growth. J. Geophys. Res. Solid Earth 121 (5), 3666–3685.
Piegari, E., Camanni, G., Mercurio, M., Marzocchi, W., 2024. Illuminating the Hierarchical Segmentation of Faults through an Unsupervised Learning Approach applied to clouds of earthquake hypocenters. In press in *Earth and Space Science* 11. https://doi.org/10.1029/2023EA003267.
Pratt, T.L., Dolan, J.F., Odum, J.K., Stephenson, W.J., Williams, R.A., Templeton, M.E., 1998. Multiscale seismic imaging of active fault zones for hazard assessment: a case study of the Santa Monica fault zone, Los Angeles, California. Geophysics 63 (2), 479–489.
Ramos, G.V., Vasconcelos, D.L., Marques, F.O., de Castro, D.L., Nogueira, F.C., Bezerra, F.H., Medeiros, V.C., 2022. Relations between inherited basement fabric and fault nucleation in a continental setting: the Rio do Peixe Basin, NE Brazil. Mar. Pet. Geol. 139, 105635.
Reasenberg, P.A., 1985. FPFIT, FPPLOT, and FPPAGE: Fortran computer programs for calculating and displaying earthquake fault-plane solutions. US Geol. Surv. Open-File Rep. 85–739.
Roche, V., Childs, C., Madritsch, H., Camanni, G., 2020. Layering and structural inheritance controls on fault zone structure in three dimensions: a case study from the northern Molasse Basin, Switzerland. J. Geol. Soc. 177 (3), 493–508.
Roche, V., Camanni, G., Childs, C., Manzocchi, T., Walsh, J., Conneally, J., Delogkos, E., 2021. Variability in the three-dimensional geometry of segmented normal fault surfaces. Earth Sci. Rev. 216, 103523.
Ross, Z.E., Ben-Zion, Y., 2014. Automatic picking of direct P, S seismic phases and fault zone head waves. Geophys. J. Int. 199 (1), 368–381.
Ross, Z.E., Trugman, D.T., Hauksson, E., Shearer, P.M., 2017. Searching for hidden earthquakes in Southern California. Science 356 (6343), 1162–1164. https://doi.org/10.1126/science.aam6399.
Ross, Z.E., Idini, B., Jia, Z., Stephenson, O.L., Zhong, M., Wang, X., Jung, J., 2019. Hierarchical interlocked orthogonal faulting in the 2019 Ridgecrest earthquake sequence. Science 366 (6463), 346–351.
Sato, H., 1994. The relationship between late Cenozoic tectonic events and stress field and basin development in Northeast Japan. J. Geophys. Res. Solid Earth 99 (B11), 22261–22274.
Sato, H., 1996. Inversion tectonics of Japanese Islands. Active Fault Res 15, 128–132.
Sato, H., Iwasaki, T., Kawasaki, S., Ikeda, Y., Matsuta, N., Takeda, T., Kawanaka, T., 2004. Formation and shortening deformation of a back-arc rift basin revealed by deep seismic profiling, Central Japan. Tectonophysics 388 (1–4), 47–58.
Satriano, C., Kiraly, E., Bernard, P., Vilotte, J.P., 2012. The 2012 Mw 8.6 Sumatra earthquake: evidence of westward sequential seismic ruptures associated to the reactivation of a N-S Ocean fabric. Geophys. Res. Lett. 39 (15).
Savran, W.H., Olsen, K.B., 2020. Kinematic rupture generator based on 3-D spontaneous rupture simulations along geometrically rough faults. J. Geophys. Res. Solid Earth 125 (10) e2020JB019464.
Schaff, D.P., Bokelmann, G.H., Beroza, G.C., Waldhauser, F., Ellsworth, W.L., 2002. High-resolution image of Calaveras fault seismicity. J. Geophys. Res. Solid Earth 107 (B9), ESE–5.
Scholz, C.H., 2010. The Mechanics of Earthquakes and Faulting. Cambridge University Press.
Scognamiglio, L., Tinti, E., Casarotti, E., Pucci, S., Villani, F., Cocco, M., Dreger, D., 2018. Complex fault geometry and rupture dynamics of the MW 6.5, 30 October 2016, Central Italy earthquake. J. Geophys. Res. Solid Earth 123 (4), 2943–2964.
Scotto di Uccio, F., Scala, A., Festa, G., Picozzi, M., Beroza, G.C., 2023. Comparing and integrating artificial intelligence and similarity search detection techniques: application to seismic sequences in Southern Italy. Geophys. J. Int. 233 (2), 861–874.
Scotto di Uccio, F., Lomax, A., Natale, J., Muzellec, T., Festa, G., Nazeri, S., Zollo, A., 2024. Delineation and fine-scale structure of fault zones activated during the 2014–2024 unrest at the Campi Flegrei caldera (Southern Italy) from high-precision earthquake locations. Geophys. Res. Lett. 51 (12) e2023GL107680.
Seebeck, H., Tenthorey, E., Consoli, C., Nicol, A., 2015. Polygonal faulting and seal integrity in the Bonaparte Basin, Australia. Mar. Pet. Geol. 60, 120–135.
Spallarossa, D., Cattaneo, M., Scafidi, D., Michele, M., Chiaraluce, L., Segou, M., Main, I. G., 2021. An automatically generated high-resolution earthquake catalogue for the 2016–2017 Central Italy seismic sequence, including P and S phase arrival times. Geophys. J. Int. 225 (1), 555–571.
Stabile, T.A., Vlček, J., Wcisło, M., Serlenga, V., 2021. Analysis of the 2016–2018 fluid-injection induced seismicity in the High Agri Valley (Southern Italy) from improved detections using template matching. Sci. Rep. 11 (1), 20630.
Stein, R.S., 1999. The role of stress transfer in earthquake occurrence. Nature 402 (6762), 605–609. https://doi.org/10.1038/45144.

Stirling, M.W., Wesnousky, S.G., Shimazaki, K., 1996. Fault trace complexity, cumulative slip, and the shape of the magnitude-frequency distribution for strike-slip faults: a global survey. Geophys. J. Int. 124 (3), 833–868.
Taira, A., 2001. Tectonic evolution of the Japanese island arc system. Annu. Rev. Earth Planet. Sci. 29 (1), 109–134.
Takano, O., 2002. Changes in depositional systems and sequences in response to basin evolution in a rifted and inverted basin: an example from the Neogene Niigata-Shin'etsu basin, Northern Fossa Magna, Central Japan. Sediment. Geol. 152 (1–2), 79–97.
Takeda, T., Sato, H., Iwasaki, T., Matsuta, N., Sakai, S.I., Iidaka, T., Kato, A., 2004. Crustal structure in the northern Fossa Magna region, Central Japan, modeled from refraction/wide-angle reflection data. Earth Planets Space 56, 1293–1299.
Toda, S., Stein, R.S., Richards-Dinger, K., Bozkurt, S.B., 2005. Forecasting the evolution of seismicity in southern California: Animations built on earthquake stress transfer. J. Geophys. Res. Solid Earth 110 (B5), B05S16. https://doi.org/10.1029/2004JB003415.
Toda, S., Stein, R.S., Sevilgen, V., Lin, J., 2011. Coulomb 3.3 Graphic-rich deformation and stress-change software for earthquake, tectonic, and volcano research and teaching—user guide. US Geological Survey open-file report 1060 (2011), 63.
Tondi, E., Jablonská, D., Volatili, T., Michele, M., Mazzoli, S., Pierantoni, P.P., 2020. The Campotosto linkage fault zone between the 2009 and 2016 seismic sequences of Central Italy: Implications for seismic hazard analysis. GSA Bull. 133 (7–8), 1679–1694. https://doi.org/10.1130/B35788.1.
Tung, S., Sippl, C., Shirzaei, M., Taymaz, T., Masterlark, T., Medved, I., 2024. Structural controls on fault slip models of the 6 February 2023 Kahramanmaraş, Türkiye earthquake doublet with finite element analyses. Geophys. Res. Lett. 51 (16) e2023GL107472.
Tvedt, A.B., Rotevatn, A., Jackson, C.A.L., Fossen, H., Gawthorpe, R.L., 2013. Growth of normal faults in multilayer sequences: a 3D seismic case study from the Egersund Basin, Norwegian North Sea. J. Struct. Geol. 55, 1–20.
Valentini, A., DuRoss, C.B., Field, E.H., Gold, R.D., Briggs, R.W., Visini, F., Pace, B., 2020. Relaxing segmentation on the Wasatch fault zone: Impact on seismic hazard. Bull. Seismol. Soc. Am. 110 (1), 83–109.
Waldhauser, F., Ellsworth, W.L., 2000. A double-difference earthquake location algorithm: Method and application to the northern Hayward fault, California. Bull. Seismol. Soc. Am. 90 (6), 1353–1368.
Waldhauser, F., Schaff, D.P., 2008. Large-scale relocation of two decades of Northern California seismicity using cross-correlation and double-difference methods. J. Geophys. Res. Solid Earth 113 (B8).
Walsh, J.J., Watterson, J., 1989. Displacement gradients on fault surfaces. J. Struct. Geol. 11 (3), 307–316.
Walsh, J.J., Bailey, W.R., Childs, C., Nicol, A., Bonson, C.G., 2003. Formation of segmented normal faults: a 3-D perspective. J. Struct. Geol. 25 (8), 1251–1262.
Wesnousky, S.G., 1988. Seismological and structural evolution of strike-slip faults. Nature 335 (6188), 340–343.
Wesnousky, S.G., 2006. Predicting the endpoints of earthquake ruptures. Nature 444 (7117), 358–360.
Wesnousky, S.G., 2008. Displacement and geometrical characteristics of earthquake surface ruptures: issues and implications for seismic-hazard analysis and the process of earthquake rupture. Bull. Seismol. Soc. Am. 98 (4), 1609–1632.
Williams, G.D., Powell, C.M., Cooper, M.A., 1989. Geometry and kinematics of inversion tectonics. Geol. Soc. Lond. Spec. Publ. 44 (1), 3–15.
Worthington, R.P., Walsh, J.J., 2017. Timing, growth and structure of a reactivated basin-bounding fault. Geol. Soc. Lond. Spec. Publ. 439 (1), 511–531.
Yamaji, A., 1990. Rapid intra-arc rifting in Miocene Northeast Japan. Tectonics 9 (3), 365–378.
Zollo, A., Caruso, A., De Landro, G., Colombelli, S., Elia, L., 2021. A Bayesian Method for Real-Time Earthquake Location using Multiparameter Data. J. Geophys. Res. Solid Earth 126 (3) e2020JB020359.